AD-A041 974 OHIO STATE UNIV COLUMBUS ELECTROSCIENCE LAB F/G 9/5
A GTD ANALYSIS OF THE RADIATION FROM SLOTS IN PLANAR AND CYLIND--ETC(U)
FEB 77 P H PATHAK F19628-76-C-0154
UNCLASSIFIED ESL-4396-2 RADC-TR-77-156 NL

1 OF 1
AD A041974

END

DATE FILMED
8 - 77

RADC-TR-77-156
Final Technical Report
February 1977

AD A041974

A GTD ANALYSIS OF THE RADIATION FROM SLOTS IN PLANAR AND CYLINDRICAL PERFECTLY-CONDUCTING STRUCTURES WITH A SURFACE IMPEDANCE PATCH

P. H. Pathak

DDC
RECEIVED
JUL 21 1977
C

Approved for public release;
distribution unlimited

ROME AIR DEVELOPMENT CENTER
AIR FORCE SYSTEMS COMMAND
GRIFFISS AIR FORCE BASE, NEW YORK 13441

AD No.
DDC FILE COPY

This report has been reviewed by the RADC Information Office (OI) and is releasable to the National Technical Information Service (NTIS). At NTIS it will be releasable to the general public, including foreign nations.

This technical report has been reviewed and approved for publication.

APPROVED:

NICHOLAS P. KERNWEIS
Project Engineer

APPROVED: ALLAN C. SCHELL
Acting Chief
Electromagnetic Sciences Division

FOR THE COMMANDER:

Plans Office

UNCLASSIFIED

SECURITY CLASSIFICATION OF THIS PAGE (When Data Entered)

REPORT DOCUMENTATION PAGE	READ INSTRUCTIONS BEFORE COMPLETING FORM
1. REPORT NUMBER: RADC-TR-77-156	2. GOVT ACCESSION NO.
3. RECIPIENT'S CATALOG NUMBER	
4. TITLE (and Subtitle): A GTD ANALYSIS OF THE RADIATION FROM SLOTS IN PLANAR AND CYLINDRICAL PERFECTLY-CONDUCTING STRUCTURES WITH A SURFACE IMPEDANCE PATCH,	5. TYPE OF REPORT & PERIOD COVERED: Final Report 15 March 1976 – 6 Jan 1977
	6. PERFORMING ORG. REPORT NUMBER: ESL-4396-2
7. AUTHOR(s): P. H. Pathak	8. CONTRACT OR GRANT NUMBER(s): Contract F19628-76-C-0154
9. PERFORMING ORGANIZATION NAME AND ADDRESS: The Ohio State University ElectroScience Laboratory, Department of Electrical Engineering Columbus, Ohio 43212	10. PROGRAM ELEMENT, PROJECT, TASK AREA & WORK UNIT NUMBERS: 62702F 46001101
11. CONTROLLING OFFICE NAME AND ADDRESS: Deputy for Electronic Technology (RADC/ETER) Hanscom AFB, MA 01731 Contract Monitor: Nicholas P. Kernweis, ETER	12. REPORT DATE: February 1977
	13. NUMBER OF PAGES: 75 (73 p.)
14. MONITORING AGENCY NAME & ADDRESS (if different from Controlling Office)	15. SECURITY CLASS. (of this report): Unclassified
	15a. DECLASSIFICATION/DOWNGRADING SCHEDULE

16. DISTRIBUTION STATEMENT (of this Report)

Approved for public release; distribution unlimited

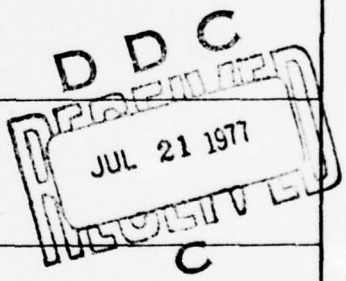

17. DISTRIBUTION STATEMENT (of the abstract entered in Block 20, if different from Report)

18. SUPPLEMENTARY NOTES

19. KEY WORDS (Continue on reverse side if necessary and identify by block number)

Geometrical Theory of Diffraction (GTD)
Impedance Surface
Slots in planar and cylindrical perfectly-conducting surfaces covered with an impedance surface patch.

20. ABSTRACT (Continue on reverse side if necessary and identify by block number)

A theoretical approach based on the geometrical theory of diffraction (GTD) is employed to analyze the fields radiated by thin slots in perfectly-conducting infinite planar, and electrically large circular cylindrical structures which are covered with an impedance surface patch. The solution to these antenna problems is built up from the solutions to several, appropriate canonical problems. The total field radiated by the slot is composed of the fields of rays which emanate from the slot to the

DD FORM 1 JAN 73 1473 EDITION OF 1 NOV 65 IS OBSOLETE

UNCLASSIFIED

SECURITY CLASSIFICATION OF THIS PAGE (When Data Entered)

19.

Surface waves
Elliot mode field
Surface wave diffraction
Canonical problems
Uniform approximations in transition regions

20.

observation point via points of diffraction on the surface, in addition to the direct ray path. The type of impedance surface chosen is such that the slot excites a bound surface wave mode on the flat impedance surface patch for the planar case, whereas it excites an Elliot type mode on the curved impedance patch for the circular cylinder case. The GTD solution not only imparts a physical insight into the radiation mechanisms involved, but it is also efficient for numerical calculations. Some numerical results based on this initial GTD analysis are presented, and are seen to agree well with the results obtained by other approaches.

EVALUATION

1. This report is the Final Report on the contract. It covers research done on radiation from thin slots in perfectly-conducting planar and cylindrical structures during the 11 month period 15 March 1976 to 6 January 1977. The work deals with a geometrical theory of diffraction analysis of high frequency radiation from thin slots in perfectly-conducting planar and circular cylindrical structures which are partially covered with a reactive impedance surface to enhance strong circularly polarized radiation in the vicinity of the horizon. Numerical results and analytical expression have been presented for the radiation patterns of both the transverse electric (TE) and transverse magnetic (TM) cases. Results of the geometric theory of diffraction (GTD) calculations are compared against results obtained by a combination of the method of moments (MM) and the (GTD), abbreviated as (MM-GTD). Although each is an approximate method the MM-GTD method is slightly more accurate in predicting the patterns of electromagnetic radiation for these types of antennas.

2. The present study is applicable to the problem of controlling the pattern shape of electromagnetic radiation from flush mounted antennas used in high speed aircraft, missiles or satellites.

Nicholas P. Kernweis

NICHOLAS P. KERNWEIS
Project Engineer

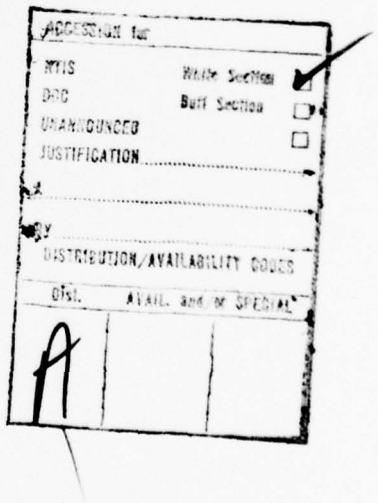

ACKNOWLEDGMENT

The author wishes to thank Professor L. Peters, Jr. ...is critical review of this manuscript.

PRECEDING PAGE BLANK-NOT FILMED

TABLE OF CONTENTS

		Page
I	INTRODUCTION	1
II	ANALYTICAL FORMULATION	5
	A. Analysis of the Planar Antenna Configuration	5
	B. Analysis of the Circular Cylinder Antenna Configuration	11
III	NUMERICAL RESULTS AND DISCUSSION	21
REFERENCES		36
Appendix		
I	AN ANALYSIS OF THE CANONICAL PROBLEM OF THE RADIATION FROM A LINE SOURCE ON AN INFINITE PLANAR IMPEDANCE SURFACE	37
II	AN ANALYSIS OF THE CANONICAL PROBLEM OF SURFACE WAVE DIFFRACTION BY A PLANAR, TWO PART IMPEDANCE SURFACE	46
III	SURFACE FIELDS IN THE CANONICAL PROBLEM OF A LINE SOURCE ON A CIRCULAR CYLINDER COMPLETELY COVERED WITH AN IMPEDANCE SURFACE	55
IV	THE RADIATION BY AN EQUIVALENT LINE SOURCE AT A DISCONTINUITY IN IMPEDANCE ON A PERFECTLY CONDUCTING CIRCULAR CYLINDER COVERED WITH AN IMPEDANCE SURFACE PATCH	63

PRECEDING PAGE BLANK-NOT FILMED

I. INTRODUCTION

This report deals with a geometrical theory of diffraction (GTD) [1] analysis of the high frequency (h.f.) radiation from slots in perfectly-conducting, planar and circular cylindrical structures which are partly covered with an impedance surface patch. The present study is applicable to the problem of controlling the pattern shape of the electromagnetic radiation from a flush mounted, airborne antenna for satellite communication purposes. In this application, a slot antenna is flush mounted in the aircraft fuselage, and the radiation pattern in the roll plane containing the slot is of interest. Consequently, the problem is essentially two-dimensional (2-D) in nature, and the aircraft fuselage may be modeled approximately by a circular cylinder in the roll plane. The effects of the aircraft wings are ignored in this initial study; however, their effects can be incorporated in the future work in a straightforward manner as will be indicated later on. In particular, it is of prime interest in the satellite communication type application for the airborne antenna to have a gain approximately that of the pattern maximum near the horizon or the shadow boundary associated with the antenna. Such a desired high gain may be achieved by an impedance loading of the perfectly-conducting surface around the slot.

The antenna configurations of interest which are analyzed in this report are illustrated in Figures 1 and 2. The slot is present in the perfectly-conducting surface and the perfectly-conducting surface is coated with a sufficiently long impedance surface patch which also covers the slot as shown in Figures 1 and 2. With a proper choice of impedance, the slot may be allowed to radiate as an end-fire antenna near the horizon; this effect may then be employed to increase the gain near the horizon. By a proper choice of the impedance, Z_s, it is implied that Z_s is chosen such that the slot can excite a bound surface wave mode on the planar impedance surface of Figure 1; whereas, it can excite an Elliot type mode [2] on the curved impedance surface of Figure 2. The Elliot mode propagates along the curved impedance surface with negligible leakage, and it corresponds in the limiting case of the infinite radius of curvature to the bound surface wave mode on the planar impedance surface. These modes on the impedance surface diffract from the ends of the impedance patch (as a result of the discontinuity in surface impedance there), thereby producing an end-fire effect. It is noted that the surface wave or Elliot type modes discussed above are excited by an axial (or $\hat{z}$-directed) slot in the configurations of Figures 1 and 2, if the surface impedance is inductive. Whereas, a circumferential (or $\hat{\tau}$-directed) slot will excite these modes only if the surface impedance is capacitive.

In the present analysis, the impedance surface patch is used to approximately simulate the effects of a thin, uniform dielectric or ferrite cover, or a properly designed corrugated surface of finite extent on the perfectly-conducting planar or cylindrical antenna structure. The slot in the perfectly-conducting structure is covered by the dielectric or ferrite material, and it is assumed that the electric field in the slot aperture is known, so that one also knows the equivalent magnetic current in the aperture. The radiation

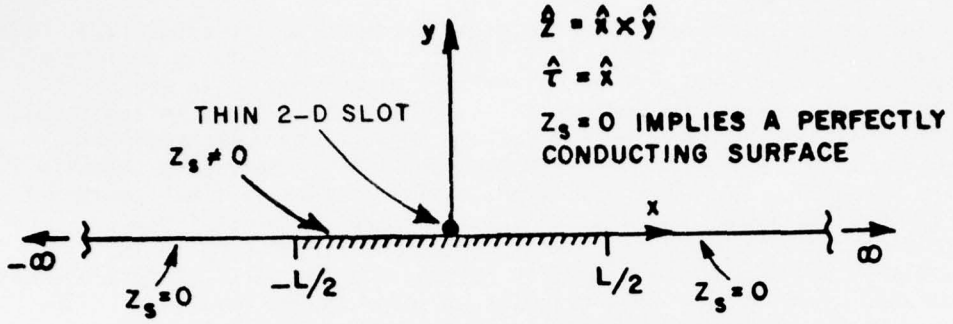

Figure 1. A thin, 2-D slot in an infinitely long, planar, perfectly-conducting structure with a surface impedance patch of length L. The value of the surface impedance is Z_S.

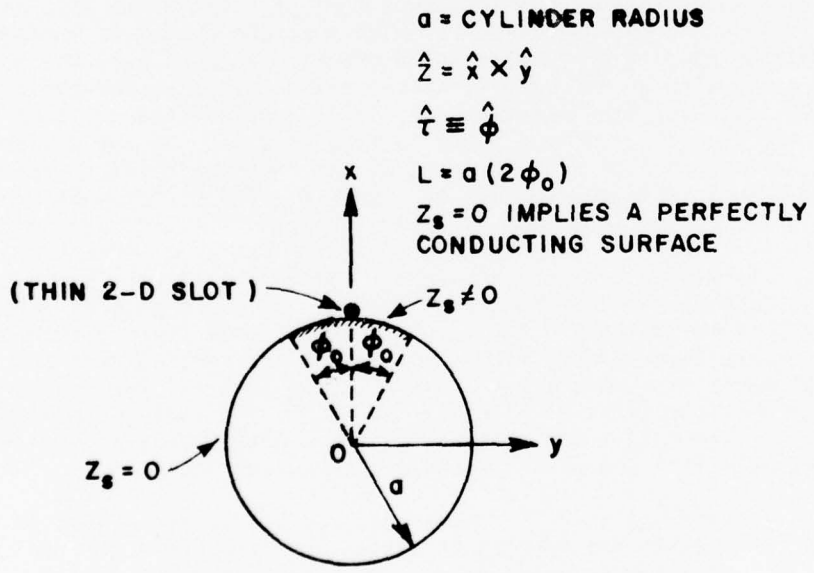

Figure 2. A thin 2-D slot in a perfectly-conducting circular cylinder with an impedance surface patch of arc length L. The value of the surface impedance is Z_S.

from a slot of finite width may be obtained by quantizing the source distribution in the aperture, and by superposing the fields radiated by each of the quantized sources. An equivalent quantized source in this case is a $\hat{z}$-directed magnetic line source for the axial slot; whereas, it is a $\hat{\tau}$-directed magnetic line dipole for the circumferential slot. These equivalent quantized magnetic currents radiate in the presence of the perfectly-conducting surface (which covers the aperture as well), and the dielectric or ferrite material which covers the perfectly-conducting surface. The strengths of the equivalent sources are weighted according to the source distribution in the aperture. In the present report, only the radiation from a magnetic line source and a magnetic line dipole will be analyzed since the radiation from a slot of finite width may be readily obtained from this analysis by superposition. In the impedance surface approximation for the truncated dielectric or ferrite cover on the perfectly-conducting surface, the equivalent problem to be analyzed consists of an equivalent magnetic line or line dipole source on the impedance surface patch which covers the perfectly-conducting planar or cylindrical surface.

While the cylindrical antenna configuration of Figure 2 is important in this study because it models an aircraft fuselage in the roll plane, the planar configuration of Figure 1 is also analyzed in this report because it is a more basic geometrical configuration involving a perfectly-conducting structure with a surface impedance patch, and because a comparison of the patterns for the configurations in Figures 1 and 2 allows one to ascertain the effects of surface curvature especially in the region of space in which the slot is directly visible (i.e., the lit region).

A GTD analysis has been performed previously with success to analyze the radiation from slots in truncated, planar dielectric covered surfaces [3], hence it was decided to extend the GTD analysis of [3] to treat the problems in Figures 1 and 2. In particular, the GTD solutions to the problems in Figures 1 and 2 are "built up" from the asymptotic h.f. solutions to several, appropriate canonical problems as in [3], however the type of canonical problems analyzed and employed in this report are quite different from the ones employed in [3]. The significant advantages of the GTD method, which is an asymptotic h.f. method, are that once the pertinent GTD launching, propagation and diffraction coefficients are known from the solutions to canonical problems (or by some other means), then the GTD may be used to calculate the fields radiated, scattered, or diffracted from complex structures in a simple fashion by appropriately expressing the fields in terms of the above mentioned coefficients together with the spatial divergence factors for the rays associated with these fields. Such a ray description results from the local nature of propagation, scattering, and diffraction which is exhibited by asymptotic h.f. field approximations. The spatial divergence factors for the rays indicate the presence and the locations of the caustics of the ray system. Generally one of the caustics of the diffracted ray occurs at the point of diffraction on the surface. Away from the point of diffraction, the diffracted ray tube spreads according to the laws of

ordinary geometrical optics. The launching or diffraction coefficients provide the starting amplitudes of the rays directly emanated from the source, or the rays diffracted from certain points of diffraction on the surface, respectively. Therefore, in addition to the usual rays of geometrical optics corresponding to the incident and reflected rays which propagate from the source to the observation point along direct and reflected ray paths, respectively, the diffracted rays propagate from the source to the observation point via points of diffraction on the surface in accordance with the generalized Fermat's principle proposed in Keller's GTD [1]. The diffracted rays are produced by the presence of discontinuities or variations in the geometrical and electrical properties of the surface (e.g., a discontinuity in surface impedance). For a comprehensive account of GTD which also includes some new and useful results for engineering applications, one is referred to Kouyoumjian [4]. The ray description for the fields not only provides a simple solution, but one which is also highly efficient for numerical computations. Furthermore, the ray contributions provide a direct physical insight into the various scattering diffraction and radiation mechanisms which are present, thereby also providing useful design information for controlling these effects advantageously.

One notes however that the ray optical field description breaks down at and in the neighborhood of caustics and shadow boundaries, hence the ray field must either be modified or supplemented by a separate solution so that it remains valid within these regions of space which are commonly referred to as transition regions. The field analysis in the transition region is complicated because the fields must change rapidly but smoothly across these regions. Modifications or the introduction of supplemental solutions to the ray field within the transition regions are referred to as uniform representations if they not only remain valid within these transition regions, but if they also reduce to the proper ray fields outside the transition regions. There are no ray caustics in the far zone of the sources in the antenna configurations of Figures 1 and 2, respectively; however, shadow boundaries are present for the circular cylinder antenna configuration of Figure 2 due to the finite radius of curvature of the cylinder in this case. Such shadow boundaries are absent in the planar configuration of Figure 1. Hence, a uniform asymptotic approximation is developed in the present analysis for the cylindrical antenna configuration of Figure 2 to provide field expressions which are valid within the transition regions, and which reduce uniformly to the ray fields outside these regions.

The analytical details are presented in Section II. Some preliminary numerical results for the radiation patterns are illustrated in Section III for both, axial and circumferential slots in the geometrical configurations of Figures 1 and 2, respectively. The solutions to the various canonical problems from which the final GTD solution is constructed are indicated in the Appendices. Some useful modifications, refinements, and generalizations of this work which are worth pursuing are also discussed in Section III.

II. ANALYTICAL FORMULATION

The ray optical analysis based on the GTD for the antenna configurations of Figures 1 and 2 will be indicated in this section. Specifically, the manner in which the analysis of the composite problems in Figures 1 and 2 will be built up or constructed from the asymptotic solutions to somewhat simpler canonical problems will be indicated. Basically, the total radiated field is composed of the fields associated with rays which propagate not only directly from the source to the observation point, but also with rays which propagate via points on the surface at which variations or discontinuities in the geometrical and electrical properties can occur. Such points constitute points of diffraction on the surface.

The planar configuration of Figure 1 will be analyzed first in Section A, and the analysis for the cylindrical configuration of Figure 2 will follow in Section B. Both, the axial and circumferential slot cases will be considered in Sections A and B. It is noted that due to the 2-D nature of the problem, an axial slot in the configurations of Figures 1 and 2 radiates only a $\hat{z}$ component of the magnetic field which will be denoted by H_z; whereas, a circumferential slot in these configurations radiates only a $\hat{z}$ component of the electric field which will be denoted by E_z. The solution for the axial slot case may be referred to as the TE_z solution, and likewise the solution for the circumferential slot case may be referred to as the TM_z solution.

As mentioned previously in Section I, only the radiation from a magnetic line source (for the TE_z case) and the magnetic line dipole source (for the TM_z case) on an impedance surface patch which covers a perfectly-conducting planar or circular cylindrical surface will be analyzed in this report; these magnetic line currents constitute the quantized, equivalent sources in the axial and circumferential slot apertures. The radiation from a 2-D axial or circumferential slot of finite width may be readily obtained from this analysis via superposition. In the impedance surface approximation for the truncated dielectric or ferrite cover on the perfectly-conducting surface, the equivalent problems to be analyzed therefore consist of an equivalent magnetic line or line dipole source on an impedance surface patch which covers the perfectly-conducting planar and cylindrical surfaces, respectively.

An $e^{j\omega t}$ time convention is assumed and suppressed in the following analysis unless specified otherwise (as in Appendix II).

A. Analysis of the Planar Antenna Configuration

According to the GTD, one may simply describe the field radiated by the planar antenna configuration of Figure 1 in terms of a superposition of the fields associated with the rays which are directly radiated by the source at O, and the rays which are diffracted from the ends of the surface impedance patch at Q_1 and Q_2, respectively. The pertinent rays for this problem are illustrated in Figure 3 in which u^r represents the field of the ray directly radiated from a line source

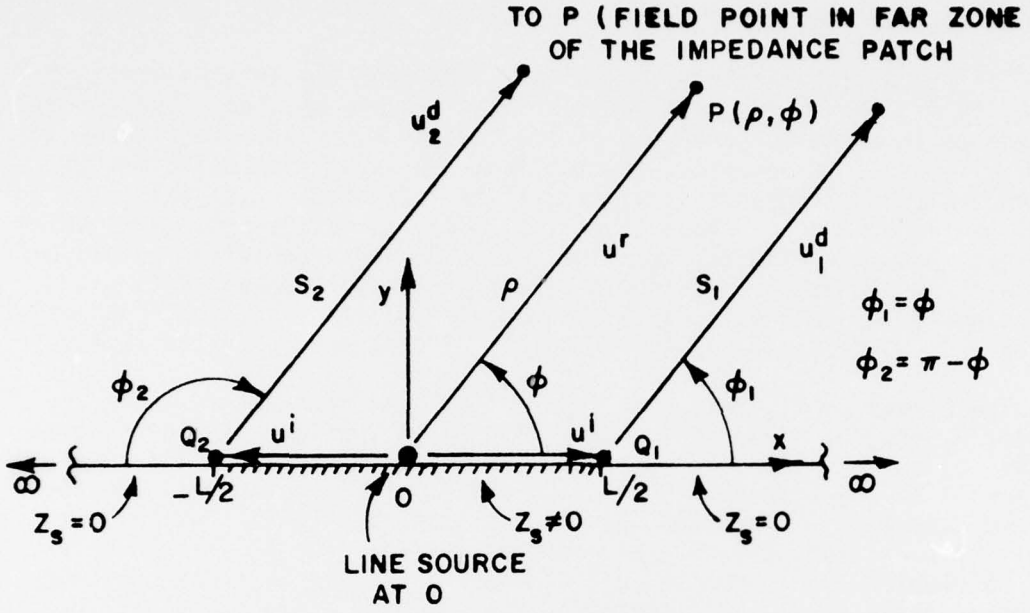

Figure 3. Rays associated with the radiation from a line source on an infinite, planar perfectly-conducting surface which is covered with an impedance surface patch.

at 0, whereas u_1^d and u_2^d represent the fields diffracted from the ends Q_1 and Q_2 of the surface impedance patch, respectively. The surface impedance, Z_s is chosen to support a bound surface wave type mode which is excited by the line source at 0. Thus the surface impedance, Z_s is inductive for the magnetic line source case (corresponding to the axial slot, or TE_z case), whereas Z_s is capacitive for the magnetic line dipole source (corresponding to the circumferential slot, or TM_z case). The field of this bound surface wave mode is denoted by u^i; this field propagates from the source at 0 to the ends of the surface impedance patch at Q_1 and Q_2, respectively as shown in Figure 3, Since there is a discontinuity in surface impedance at Q_1 and Q_2, the field u^i at $Q_{1,2}$ is partly reflected, and partly diffracted from $Q_{1,2}$. Thus, $u^q_{1,2}$ is produced via the diffraction of the surface wave field $u^i(Q_{1,2})$ when it impinges upon the surface impedance discontinuity at $Q_{1,2}$. Of course, multiple reflections of the surface wave field can occur between the ends Q_1 and Q_2, and the inclusion of these multiple reflection-diffraction effects is discussed later in Section III. It is assumed in the present analysis that the surface impedance patch is sufficiently large in extent so that only the bound surface wave mode field u^i (which is a non-radiating field) constitutes the dominant contributor to the field on the impedance

surface far from the source, since the field u^r (i.e., the radiated or space wave field) becomes vanishingly small along the surface impedance boundary when it is evaluated far from the source. This assumption may be verified by solving the canonical problem of a line source on an infinite, planar impedance surface as shown in Figure 4. The canonical problem of Figure 4 is briefly analyzed in Appendix I, and the solution to this problem provides the necessary expressions for the fields u^r and u^i of Figure 3.

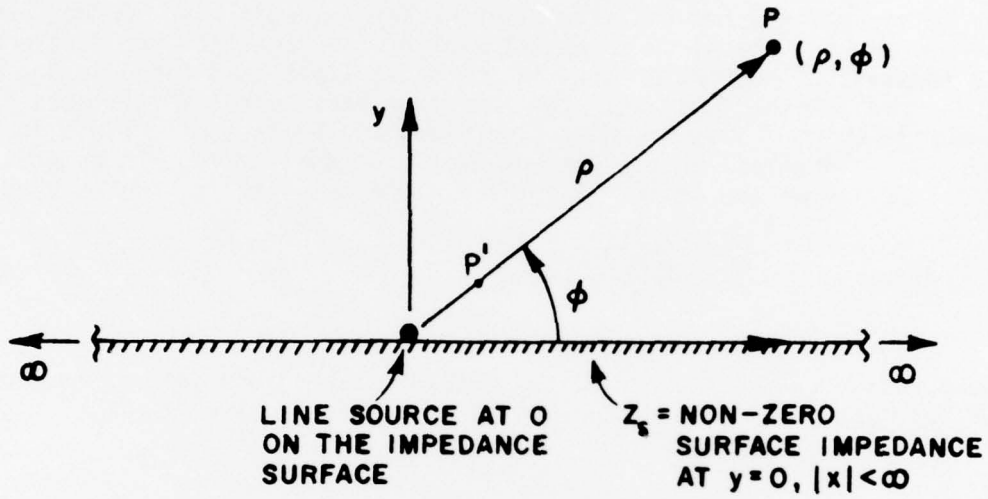

Figure 4. Geometry of the canonical problem of a line source on an infinite, planar impedance surface.

In the radiation pattern analysis, the field point P is assumed to be in the far zone of the surface impedance patch. The field $u^r(P)$, which is the field u^r evaluated at P is a cylindrical wave type field which emanates from the line source at O when P is sufficiently far from O; this field may be represented according to geometrical optics as

$$u^r(P) \sim u^r(P') \sqrt{\frac{\rho^r}{\rho^r + [PP']}}\; e^{-jk[PP']} \qquad (1)$$

where P' is some reference point* on the ray path from O to P, and k is the free space wave number. The caustic distance ρ^r of this ray is simply the distance OP'. In order to relate the field $u^r(P)$ to the source, one must take the limit of the RHS of Equation (1) as $\rho^r \to 0$ (or P' approaches the point O). In the ray approximation, $u^r(P')$ is singular

*The quantity $\overline{PP'}$ in Equation (1) denotes the distance from P' to P.

at the caustic, but the limit of $\sqrt{\rho^r}\, u^r(P')$ as $\rho^r \to 0$ exists, and it is proportional to the strength of the magnetic line source or the magnetic line dipole source at O and the radiation coefficient R which is defined below. Let $\bar{M} = \hat{u} M\, \delta(x)\delta(y)$ denote this magnetic line source, or the magnetic line dipole source so that

$$\lim_{\rho^r \to 0} \sqrt{\rho^r}\, u^r(P') \propto M R \quad . \tag{2}$$

One notes that $\hat{u}=\hat{z}$ for the axial slot or the magnetic line source case, whereas $\hat{u}=\hat{x}$ for the circumferential slot or the magnetic line dipole case. The constant of proportionality in the above limit is defined as C_o, where C_o is some complex constant. The radiation coefficient R indicates the manner in which the source M at O distributes the radiation field in space; thus, R is identical to the pattern factor of the source. In general, R is a function of the azimuthal angle ϕ. One notes that $PP' \to \rho$ as $\rho^r \to 0$, so

$$u^r(P) \sim C_o\, M\, R(\phi)\, \frac{e^{-jk\rho}}{\sqrt{\rho}} \tag{3}$$

The constant C_o and the radiation coefficient $R(\phi)$ are determined from the solution to the canonical problem of Figure 4, as given in Appendix I.

$$C_o = \begin{cases} -\sqrt{\dfrac{jk}{4\pi}}\,, & \text{for the magnetic line dipole, or } TM_z \text{ case} \\ -Y_o\sqrt{\dfrac{jk}{4\pi}}\,, & \text{for the magnetic line source, or } TE_z \text{ case.} \end{cases} \tag{4}$$

The Y_o in Equation (4) is the free space admittance. $R(\phi)$ will be different for the magnetic line source, and the magnetic line dipole; the explicit form of this coefficient will be indicated later.

The fields $u_1^d(P)$ and $u_2^d(P)$ at P which are diffracted from the ends of the surface impedance patch at Q_1 and Q_2, respectively may be assumed to be produced by localized equivalent magnetic line sources or line dipoles at these ends. Thus, $u_{1,2}^d(P)$ may also be expressed in terms of a cylindrical ray divergence factor via ray optics as

$$u_{1,2}^d(P) \sim u_{1,2}^d(P'_{1,2}) \sqrt{\frac{\rho_{1,2}^d}{\rho_{1,2}^d + [P'_{1,2}P]}}\; e^{-jkP'_{1,2}P} \tag{5}$$

where P'_1 is some reference point between Q_1 and P; likewise P'_2 is some reference point between Q_2 and P. The caustic distances $\rho_{1,2}^d$ for these diffracted ray fields are simply given by $\rho_{1,2}^d = Q_{1,2}\, P'_{1,2}$. As before,

$$\lim_{\rho^d_{1,2}\to 0} \sqrt{\rho^d_{1,2}}\; u^d_{1,2}(P')$$

is finite and proportional to the strength of the equivalent line source at $Q_{1,2}$. The strength of the equivalent line source would of course be proportional to the strength of the surface wave field u^i which strikes the ends $Q_{1,2}$ to produce the diffracted field $u^d_{1,2}(P)$. Hence

$$\lim_{\rho^d_{1,2}\to 0} \sqrt{\rho^d_{1,2}}\; u^d_{1,2}(P') = u^i(Q_{1,2}) \cdot D(\phi_{1,2}),$$

where $D(\phi_{1,2})$ is the diffraction coefficient at $Q_{1,2}$ which indicates the manner in which the diffracted field is distributed in space. The functional form of D is the same at Q_1 and Q_2, respectively, and the diffraction coefficient at Q_1 depends on the angle ϕ_1; whereas, the diffraction coefficient at Q_2 depends on the angle ϕ_2. The angles ϕ_1 and ϕ_2 are indicated in Figure 3. Thus, Equation (5) becomes

$$u^d_{1,2}(P) \sim u^i(Q_{1,2})\; D(\phi_{1,2})\; \frac{e^{-jks_{1,2}}}{\sqrt{s_{1,2}}} \quad ; \quad \begin{cases} \phi_1 = \phi \\ \phi_2 = \pi - \phi \end{cases} . \tag{6}$$

It is noted that $P'_1P \to s_1$ as $\rho^d_1 \to 0$, and $P'_2P \to s_2$ as $\rho^d_2 \to 0$, in Equation (5). In the far zone, one may approximately replace

$$\frac{e^{-jks_{1,2}}}{\sqrt{s_{1,2}}} \quad \text{by} \quad \frac{e^{-jk\rho}}{\sqrt{\rho}} \cdot e^{jk\frac{L}{2}\cos\phi_{1,2}},$$

using the origin as the phase reference. Thus,

$$u^d_{1,2}(P) \sim u^i(Q_{1,2})\; D(\phi_{1,2})\; e^{jk\frac{L}{2}\cos\phi_{1,2}}\; \frac{e^{-jk\rho}}{\sqrt{\rho}} . \tag{7}$$

The incident surface wave field $u^i(Q_{1,2})$ launched by the source M at O may be represented as

$$u^i(Q_{1,2}) = C_o\, M\, L^{sw}\, e^{-j\beta\frac{L}{2}} \tag{8}$$

where L^{SW} and β are the surface wave launching and propagation coefficients, respectively; both of these quantities are found from the solution to the canonical problem of Figure 4 as given in Appendix I. The remaining quantity, $D(\phi_{1,2})$ in Equation (7) must be found from the solution to the canonical problem of Figure 5 as given in Appendix II.

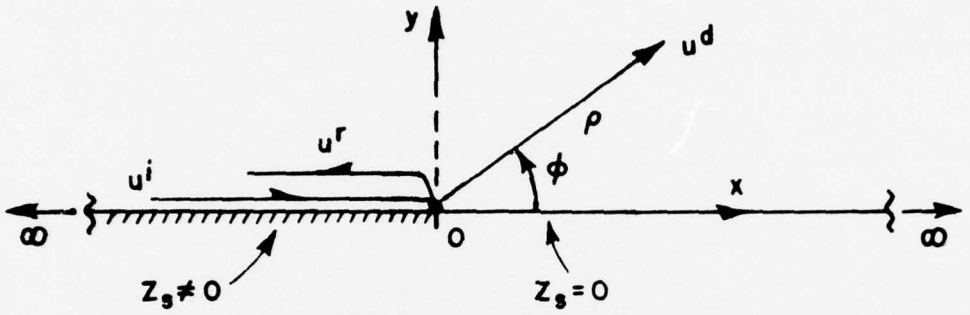

u^i = INCIDENT SURFACE WAVE MODE FIELD

u^r = REFLECTED SURFACE WAVE MODE FIELD

u^d = DIFFRACTED FIELD

Figure 5. Geometry of the canonical problem of surface wave diffraction by a discontinuity in surface impedance associated with a two part, planar impedance surface in which the surface impedance for x>0 and y=0 is zero corresponding to a perfectly-conducting boundary.

As pointed out by Keller and Karal (Journal of Appl. Phys., Vol. 31, No. 6, June 1960, pp. 1039-1046), and more recently by Felsen and Choudhary (IEEE Trans. Antennas and Propagation, Vol. AP-21, November 1973, pp. 827-842), the geometrical representation of evanescent or surface waves is by complex rays; however, since the source and field points lie on the lossless impedance surface in the calculation of $u^i(Q_{1,2})$ in this analysis, and since the field of the surface waves is not included at P, the representation in Equation (8) is adequate.

One may now specialize the above set of results to the axial slot (or TE_z) and the circumferential slot (or TM_z) cases, respectively. As mentioned previously, the magnetic current $\overline{M}$ corresponding to a quantized equivalent source in the slot is given by

$$\overline{M} = \begin{cases} \hat{z}\, M\, \delta(x)\delta(y) & \text{for the magnetic line source corresponding to the axial slot or } TM_z \text{ case.} \\ \hat{x}\, M\, \delta(x)\delta(y) & \text{for the magnetic line dipole corresponding to the circumferential slot or } TE_z \text{ case.} \end{cases} \tag{9}$$

in which M is the amplitude of the source which is assumed known and $\delta(x)\delta(y)$ is the two-dimensional Dirac delta function. The corresponding fields for the two slot types are

$$u = \begin{Bmatrix} E_z \\ H_z \end{Bmatrix} = u^r + u_1^d + u_2^d \; ; \; \text{for} \begin{Bmatrix} TM_z \\ TE_z \end{Bmatrix}, \text{ and } 0 \leq \phi \leq \pi. \tag{10}$$

The source $\overline{M}$ in Equation (9) for the TE_z and TM_z cases is explicitly defined. The quantity $R(\phi)$ in u^r for the TE_z and TM_z cases is given separately in Equations (A-26) and (A-45), respectively of Appendix I. The diffraction coefficient $D(\phi)$ appearing in $u_{1,2}^d$ above is presented separately for the TE_z and TM_z cases in Equations (A-74) and (A-97), respectively of Appendix II. One recalls that $u_{1,2}^d$ also requires an explicit knowledge of $u^i(Q_{1,2})$ which in turn requires a knowledge of L^{sw} and β as mentioned in Equation (8). These quantities are explicitly given in Appendix I by Equations (A-27) and (A-19) for the TE_z case, and by Equations (A-46) and (A-40) for the TM_z case.

B. Analysis of the Circular Cylinder Antenna Configuration

There are some essential differences between the radiation mechanisms present in the planar antenna configuration of Figure 1 which was analyzed in part A, and the cylindrical antenna configuration of Figure 2 which is analyzed below. These differences will become evident in the following discussion. As mentioned earlier, the magnetic current $\overline{M}$ corresponding to a quantized equivalent source in the slot aperture is given by

$$\overline{M} = \hat{u}\, M\, \frac{\delta(\rho-a)\,\delta(\phi)}{\rho} \; ; \quad \hat{u} = \begin{cases} \hat{z}, \text{ for the magnetic line source or the } TE_z \text{ case.} \\ \hat{\phi}, \text{ for the magnetic line dipole or the } TM_z \text{ case.} \end{cases} \tag{11}$$

The boundary SBQ' in Figure 6 constitutes the shadow boundary for the source $\overline{M}$ at Q'. The field radiated by the source $\overline{M}$ at Q' may be obtained via GTD in terms of a superposition of the fields of the rays directly radiated by the source $\overline{M}$, and the fields of the rays which are diffracted from the ends of the surface impedance patch at Q_1 and Q_2, respectively as shown in Figure 6a. The field directly radiated by $\overline{M}$ is denoted by $\tilde{u}^r$; whereas $\tilde{u}_1^d$ and $\tilde{u}_2^d$ represent the fields diffracted from Q_1 and Q_2, along direct ray paths to the observation point P, as in Figure 6a. The fields $\tilde{u}_1^d$ and $\tilde{u}_2^d$ may be assumed to be produced by equivalent magnetic line sources or line dipoles at Q_1 and Q_2, respectively. Hence, the boundaries SBQ_1 and SBQ_2 illustrated in Figure 6 correspond to the shadow boundaries of equivalent sources of the diffracted fields at Q_1 and Q_2, respectively.

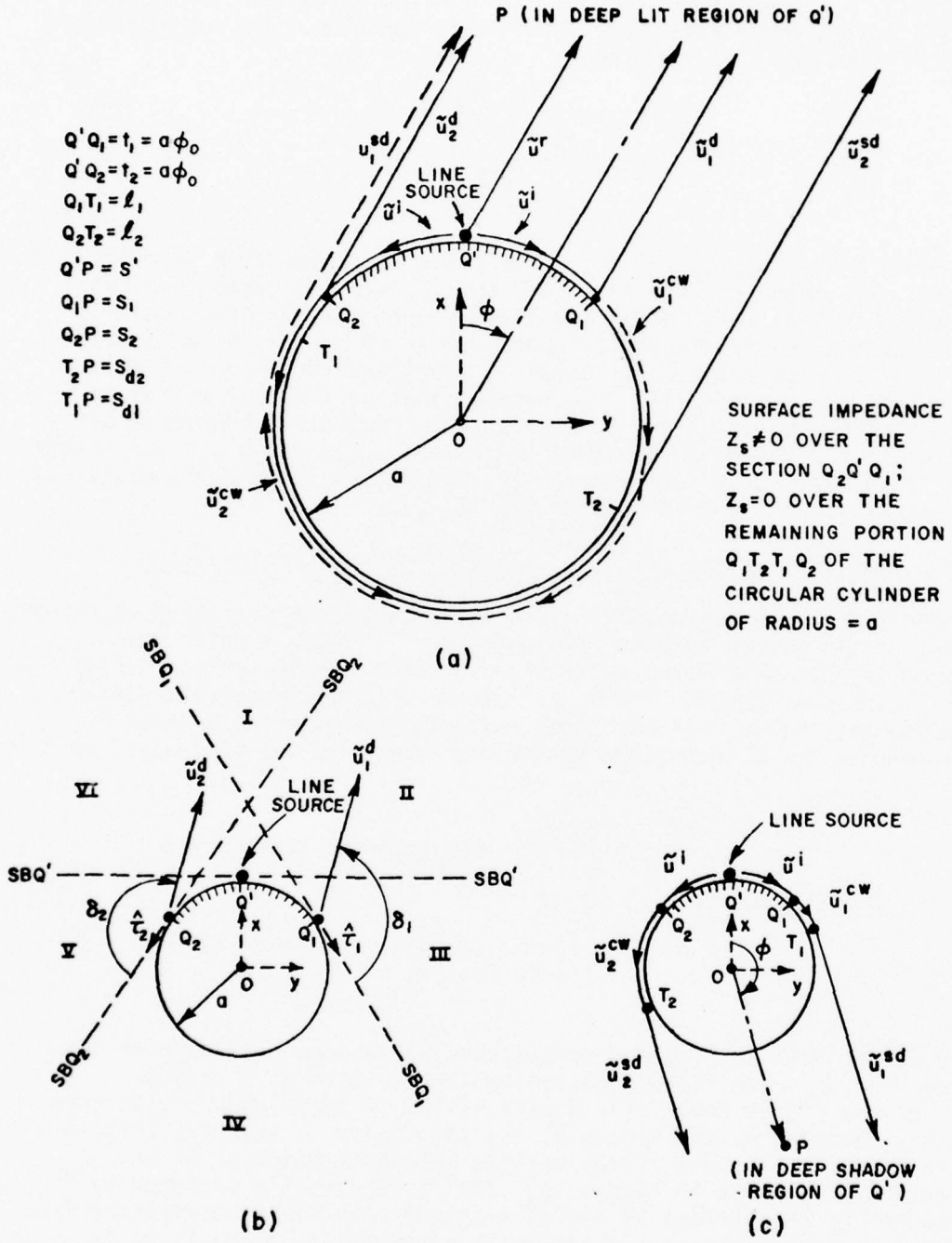

Figure 6. Rays and shadow boundaries associated with the cylindrical antenna configuration of Figure 2.

PRECEDING PAGE BLANK-NOT FILMED

As in the planar case, the type of impedance surface chosen is such that it supports an Elliot type surface wave mode which propagates along the impedance surface from the slot to the ends Q_1 and Q_2 of the patch with negligible leakage (provided the cylinder is sufficiently large). The Elliot mode field is denoted by $\tilde{u}^i$, and it's propagation path is illustrated in Figure 6. The field $\tilde{u}^i$ impinges upon the termination of the surface impedance patch at Q_1 and Q_2 to produce the diffracted fields $\tilde{u}_1^d$ and $\tilde{u}_2^d$, respectively which traverse the direct ray paths Q_1P and Q_2P to the observation point P. However, in addition to $\tilde{u}_1^d$ and $\tilde{u}_2^d$, there exist an additional class of diffracted fields resulting from the diffraction of creeping waves that are excited at Q_1 and Q_2; these creeping waves propagate over the perfectly-conducting portion of the cylinder. Sufficiently far from Q_1 and Q_2 the creeping waves are expressed in terms of a rapidly converging set of surface ray modes whose amplitudes decay exponentially due to a continuous shedding of rays from the surface ray mode fields (via surface diffraction) along the forward tangents to their surface ray paths on the perfectly-conducting part of the cylinder. These surface ray modes were introduced by Keller [1] to analyze the diffraction by smooth, convex cylinders via GTD. The surface ray modes are also commonly referred to as Watson modes [5]. The fields of the surface ray modes are denoted by $\tilde{u}_1^{cw}$ and $\tilde{u}_2^{cw}$; whereas, the fields of the rays diffracted from these surface ray modes are denoted by $\tilde{u}_1^{sd}$ and $\tilde{u}_2^{sd}$, respectively. The rays corresponding to $\tilde{u}_1^{cw}$ and $\tilde{u}_2^{cw}$ travel in opposite directions along the perfectly-conducting portion of the cylinder as shown in Figure 6. The diffracted rays corresponding to $\tilde{u}_1^{sd}$ and $\tilde{u}_2^{sd}$ are also illustrated in Figure 6. In particular, one notes that the rays corresponding to the diffracted field $\tilde{u}_{1,2}^{d}$ exist on the lit side of the shadow boundary $SBQ_{1,2}$; whereas, the rays corresponding to the diffracted field $\tilde{u}_{1,2}^{sd}$ exist on the shadow side of $SBQ_{1,2}$.

The ray descriptions $\tilde{u}_{1,2}^{d}$ and $\tilde{u}_{1,2}^{sd}$ on either side of the shadow boundary $SBQ_{1,2}$ fail at and in the neighborhood of $SBQ_{1,2}$. Therefore, a uniform approximation for the field which remains valid within this transition region adjacent to $SBQ_{1,2}$, and which reduces to $\tilde{u}_{1,2}^{d}$ and $\tilde{u}_{1,2}^{sd}$ outside the transition region in the lit and shadow sides of $SBQ_{1,2}$, respectively is presented in terms of the Fock integrals [5]. One notes that in addition to the Elliot mode field $\tilde{u}^i$ excited by $\overline{M}$ on the curved impedance patch, there also exist a set of Watson type modes which leak off energy via diffraction from the curved impedance boundary as they propagate from the source $\overline{M}$ at Q' to the ends of the impedance boundary at Q_1 and Q_2. The existence of these Watson type modes is not indicated in Figure 6 because their diffraction effects will be assumed to be negligible in comparison with those due to the Elliot type mode. The Elliot mode propagates with very little leakage, hence it may be assumed that this mode is the dominant contributor to the field on the curved impedance surface which is incident at $Q_{1,2}$. While the assumption that the leakage from the Watson type modes being small may be true only for a certain range of parameters (such as those involving the value of the surface impedance, Z_s; the length of the curved impedance surface section; and the curvature of the cylinder),

PRECEDING PAGE BLANK-NOT FILMED

the present analysis is based on this assumption being true*. There is also a transition region adjacent to the shadow boundary SBQ' associated with the source $\overline{M}$ at Q'. One notes that the ray field $\tilde{u}^r$ far from Q' vanishes along SBQ'; this may be verified via an asymptotic solution to the canonical problem of Figure 7 as given in Appendix III. Thus, since

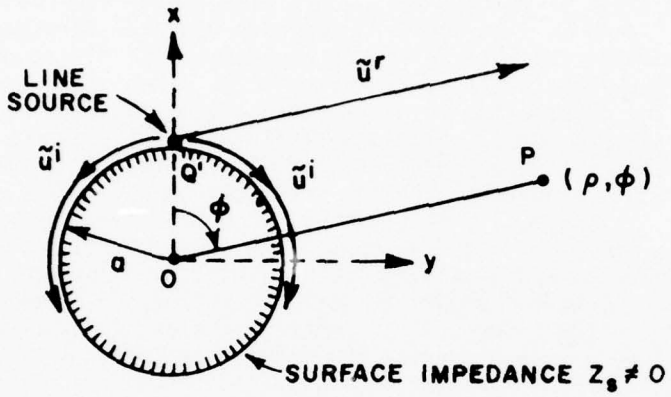

Figure 7. Geometry of the canonical problem of a line source (or thin slot) on a circular cylinder which is completely covered with an impedance surface.

the leakage or surface diffraction effects of the Watson type modes is neglected, and $\tilde{u}^r$ is continuous everywhere (even near the boundary SBQ' where it vanishes) on the lit side of SBQ' ($\tilde{u}^r \sim 0$ on the dark or shadow side of SBQ'), no uniform approximation for the fields is presented within the transition region adjacent to SBQ'. However, one would have to modify $\tilde{u}^r$ if the leakage of the Watson modes from the impedance surface is included. This modification would provide a uniform approximation within the transition region adjacent to SBQ'; such a uniform approximation involves a modified Fock integral. One notes that the inclusion of the Watson modes also requires that their diffraction from the ends of the impedance patch at Q_1 and Q_2 be included. Furthermore, a uniform approximation to the diffraction of these Watson modes from $Q_{1,2}$ must then be included within the transition regions adjacent to $SBQ_{1,2}$; otherwise, a discontinuity in the field pattern would result across $SBQ_{1,2}$. The inclusion of the effects of these Watson type modes on the curved impedance section is proposed as part of the future work dealing with refinements and extensions to the present work.

By dividing the space surrounding the cylinder into six regions as indicated in Figure 6, one notes that the total field $\tilde{u}$ radiated by the slot may be given within each of these regions I, II, III, IV, V, and VI, respectively, in terms of the ray fields $\tilde{u}^r$, $\tilde{u}^d_1$, and $\tilde{u}^{sd}_{1,2}$ as follows.

2

*One might expect this assumption to be fairly accurate for sufficiently large cylinders and for impedance patch lengths which are small in comparison to the size of the cylinder.

$$\tilde{u} = \begin{cases} \tilde{u}^r + \tilde{u}_1^d + \tilde{u}_2^d + \tilde{u}_1^{sd} + \tilde{u}_2^{sd} & , \text{ in region I} \\ \tilde{u}^r + \tilde{u}_1^d + \tilde{u}_2^{sd} & , \text{ in region II} \\ \tilde{u}_1^d + \tilde{u}_2^{sd} & , \text{ in region III} \\ \tilde{u}_1^{sd} + \tilde{u}_2^{sd} & , \text{ in region IV} \\ \tilde{u}_1^{sd} + \tilde{u}_2^d & , \text{ in region V} \\ \tilde{u}^r + \tilde{u}_1^{sd} + \tilde{u}_2^d & , \text{ in region VI} \end{cases} \tag{12}$$

As noted previously, $\tilde{u} = E_z$ in the TM_z problem; whereas, $\tilde{u} = H_z$ in the TE_z problem.

The fields $\tilde{u}_1^{cw}$ and $\tilde{u}_2^{cw}$ impinge upon the discontinuities in surface impedance at Q_2 and Q_1, after being launched from Q_1 and Q_2, respectively, thereby giving rise to further reflections and diffractions. However, these diffraction and reflections of $\tilde{u}_1^{cw}$ and $\tilde{u}_2^{cw}$ from Q_2 and Q_1, respectively are neglected in the present analysis since the fields $\tilde{u}_{1,2}^{cw}$ are exponentially decaying fields, and for sufficiently large excursions of the ray paths from Q_1 to Q_2, and vice versa, over the perfectly conducting portion, the fields $\tilde{u}_{1,2}^{cw}$ are small enough to where their diffraction effects at $Q_{2,1}$ become even smaller. The cylinder is taken to be sufficiently large electrically in the present analysis, so that the diffraction of $\tilde{u}_{1,2}^{cw}$ from $Q_{2,1}$ is indeed negligible in comparison to the other diffraction effects being considered. Also, multiple reflections of the Elliot mode field $\tilde{u}^1$ can occur between Q_1 and Q_2 on the impedance surface. The inclusion of these multiple reflection-diffraction effects is discussed later in Section III.

The fields $\tilde{u}^r$ and $\tilde{u}^i$ whose ray paths are indicated in Figure 6 may be found from the solution to the canonical problem of Figure 7 as given in Appendix III. Following the representation for $\tilde{u}^r$ for the flat surface case of part A, one may likewise express $\tilde{u}^r$ ray-optically as

$$\tilde{u}^r(P) \sim C_o \, M \, R(\phi) \frac{e^{-jks'}}{\sqrt{s'}} \quad ; \quad P \text{ in lit region of } Q'. \tag{13}$$

The distance $s' = Q'P$, and C_o has been defined earlier in Equation (4). The radiation coefficient $R(\phi)$ in Equation (13) is the same as that in Equation (3) for the planar case; this result could have been directly predicted via the geometrical optics ray approximation without having to solve for $\tilde{u}^r$ as in Appendix III. Choosing the origin as the phase reference allows one to express $\tilde{u}^r$ as

$$\tilde{u}^r(P) \sim C_o\, M\, R(\phi)\, e^{jka\cos\phi}\, \frac{e^{-jk\rho}}{\sqrt{\rho}} \quad ; \tag{14}$$

where the angle ϕ is illustrated in Figure 6.

Next, the Elliot mode field $\tilde{u}^i$ on the curved impedance surface which arrives at Q_1 or Q_2 from Q' may also be expressed in a fashion similar to $\tilde{u}^i$ for the planar case (see Equation (8)) as

$$\tilde{u}^i(Q_{1,2}) = C_o\, M\, L^{ew}\, e^{-j\gamma t_{1,2}} \quad ; \quad t_{1,2} = \text{length } Q'Q_{1,2} \quad . \tag{15}$$

The quantities L^{ew} and γ are the Elliot mode launching and propagation coefficients, respectively, which are found in Appendix III.

The field $\tilde{u}^i$ which is incident at $Q_{1,2}$ produces diffracted rays which emanate from $Q_{1,2}$ as mentioned earlier. For a sufficiently large cylinder, the nature of the diffraction of the Elliot mode from $Q_{1,2}$ may be assumed to be locally the same as that in Figure 5 for the planar, two-part impedance surface, except in the transition region adjacent to the shadow boundary $SBQ_{1,2}$ and on the shadow side of $SBQ_{1,2}$ below the transition region (wherein the surface diffracted field $\tilde{u}^{sd}_{1,2}$ is the only ray field present). However, even within the transition region adjacent to $SBQ_{1,2}$ and on the shadow side of this transition region, one may indirectly employ the surface wave diffraction coefficient for the planar case of Figure 5 to obtain an equivalent magnetic current source at $Q_{1,2}$ which in turn produces $\tilde{u}^{sd}_{1,2}$ and the transition region field. The equivalent current is a magnetic line source for the TE_z case; whereas, it is a magnetic line dipole for the TM_z case. This "equivalent" source is inhomogeneous since it is a function of δ_1 or δ_2, i.e., it depends on the aspect, ϕ, and it is regarded as the source which produces the diffracted fields. Let the equivalent magnetic current at $Q_{1,2}$ be designated as $\overline{M}^{eq}$, where

$$\overline{M}^{eq} = \begin{cases} \hat{u}_1\, M_1^{eq}(\delta_1)\, \dfrac{\delta(\rho-a)\delta(\phi-\phi_o)}{\rho} & ; \text{ at } Q_1 \\ \hat{u}_2\, M_2^{eq}(\delta_2)\, \dfrac{\delta(\rho-a)\delta(\phi+\phi_o)}{\rho} & ; \text{ at } Q_2 \end{cases} \tag{16}$$

and

$$\hat{u}_1 = \begin{Bmatrix} \hat{z}, \text{ for } TE_z \text{ case} \\ \hat{\tau}_1, \text{ for } TM_z \text{ case} \end{Bmatrix} \quad ; \quad \hat{u}_2 = \begin{Bmatrix} \hat{z}, \text{ for } TE_z \text{ case} \\ \hat{\tau}_2, \text{ for } TM_z \text{ case} \end{Bmatrix} \quad , \tag{17a,b}$$

in which $\hat{\tau}_{1,2}$ is the unit vector at $Q_{1,2}$ as shown in Figure 6. The strength $M_{1,2}^{eq}(\delta_{1,2})$ of the equivalent source $\bar{M}^{eq}$ is evaluated in Appendix IV which deals with the solution to the canonical problem of Figure 8. Since the details are presented in Appendix IV, only the

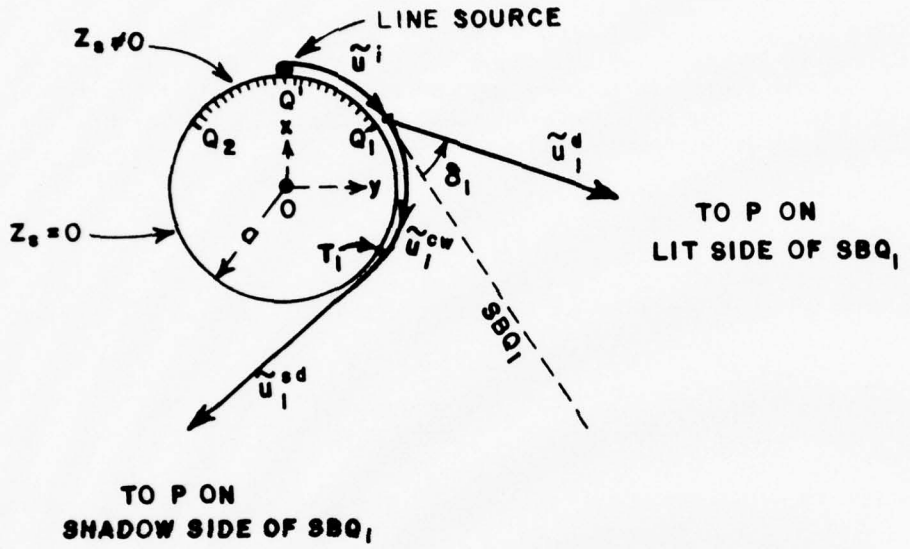

Figure 8. Geometry of the canonical problem of the diffraction of an Elliot mode by a discontinuity in surface impedance on a circular cylinder.

final results for the diffracted ray fields $\tilde{u}_{1,2}^d$ and $\tilde{u}_{1,2}^{sd}$ which are produced by $\bar{M}^{eq}$ at $Q_{1,2}$ are indicated below. One recalls that $\tilde{u}_{1,2}^d$ exists on the lit side of $SBQ_{1,2}$; whereas, $\tilde{u}_{1,2}^{sd}$ exists on the shadow side of $SBQ_{1,2}$. The ray field $\tilde{u}_{1,2}^d$ spreads cylindrically outward from $Q_{1,2}$. For the sake of brevity, the forms of $\tilde{u}_1^d$ and $\tilde{u}_1^{sd}$ will be indicated below; however $\tilde{u}_2^d$ and $\tilde{u}_2^{sd}$ have exactly similar forms (and may be obtained by replacing the subscript 1 by 2).

$$\tilde{u}_1^d(P) \sim C_o\, M_1^{eq}(\delta_1) R^{eq}(\delta_1)\, \frac{e^{-jks_1}}{\sqrt{s_1}} \quad ; \quad P \text{ in the lit side of } SBQ_1 \ . \tag{18}$$

The distances s_1 and s_2 correspond to Q_1P and Q_2P, respectively, as in Figure 6, and the angles δ_1 and δ_2 are also shown in Figure 6. The quantity $R^{eq}(\delta_1)$ is the radiation coefficient of the source

$$M_1^{eq} \frac{\delta(\rho-a)\delta(\phi-\phi_o)}{\rho}$$

at Q_1, and it is specified in Appendix IV. However, since $u_1^d(P)$ is a diffracted ray field, it is more appropriate to represent it in terms of a diffraction coefficient rather than a radiation coefficient. In fact, it is shown in Appendix IV that

$$C_o M_{1,2}^{eq} R^{eq}(\delta_{1,2}) = \tilde{u}^i(Q_{1,2})D(\delta_{1,2}) \tag{19}$$

where D is same as the diffraction coefficient in Equation (7). Thus,

$$\tilde{u}_1^d(P) \sim \tilde{u}^i(Q_1)D(\delta_1) \frac{e^{-jks_1}}{\sqrt{s_1}} \quad ; \text{ P in the lit side of SBQ}_1 \text{ (and } 0 < \delta_1 < \pi) \tag{20}$$

as in Equation (6) for the planar case. In the far zone, one may write

$$\tilde{u}_1^d(P) \sim \tilde{u}^i(Q_1)D(\delta_1) e^{jkacos(\phi-\phi_o)} \frac{e^{-jk\rho}}{\sqrt{\rho}} \quad . \tag{21}$$

One notes that $\tilde{u}_1^d \sim 0$ for $\delta_1 > \pi$; this is consistent with the assumption that the curved surface diffraction effects of the Watson type modes (excited by $\tilde{M}^{eq}$) on the curved impedance patch are negligible.

The surface diffracted ray field $\tilde{u}_{1,2}^{sd}$ excited by $M_{1,2}^{eq}(\delta_{1,2}=0)$ over the perfectly-conducting surface is given by Pathak and Kouyoumjian [6] as

$$\tilde{u}_1^{sd} \sim C_o M_1^{eq}(0) \sum_{p=1}^{N} L_p(Q_1) e^{-[\alpha_p+jk]\ell_1} D_p(T_1) \frac{e^{-jks_1}}{\sqrt{s_1}} \quad ;$$

$$\text{when P is on the shadow side of SBQ}_1. \tag{22}$$

Only $\tilde{u}_1^{sd}$ is indicated above, and $\tilde{u}_2^{sd}$ is similar to $\tilde{u}_1^{sd}$. The distance $\ell_{1,2}$ = arc length $Q_{1,2}T_{1,2}$. The distance $S_{1,2} = T_{1,2}P$ where $T_{1,2}$ is the point of diffraction or shedding of the surface diffracted ray field $\tilde{u}_{1,2}^{sd}$ and $Q_{1,2}$ is the launching point of this surface diffracted ray field

as indicated in Figure 6. L_p, D_p and α_p are the launching, diffraction and attenuation coefficients of the pth surface ray (or Watson) mode; these are discussed in [6] and are also introduced in Appendix IV. In numerical calculations, the inclusion of only the first couple of modes (p=1,2) is sufficient to obtain good accuracy provided P is outside the transition region adjacent to SBQ_1.

One may now specialize the above results to the axial slot (or TE_z) and the circumferential slot (or TM_z) cases, respectively. The magnetic current $\overline{M}$ at Q' corresponding to the two types of slots is defined in Equation (11) in which M is the amplitude of the source which is assumed known. The total field, $\tilde{u}$ radiated by the source $\overline{M}$ is obtained from Equation (12) after noting that

$$\tilde{u} = \begin{Bmatrix} E_z \\ H_z \end{Bmatrix} \quad , \quad \text{for the} \quad \begin{Bmatrix} TM_z \\ TE_z \end{Bmatrix} \quad \text{cases} \quad ; \text{ and } \quad 0 \leq \phi \leq 2\pi \ . \qquad (23)$$

The total field $\tilde{u}$ in Equation (12) is composed of $\tilde{u}^r$, $\tilde{u}^d_{1,2}$ and $\tilde{u}^{sd}_{1,2}$. The diffracted fields $\tilde{u}^d_{1,2}$ and $\tilde{u}^{sd}_{1,2}$ in turn are expressed in terms of $\tilde{u}^i(Q_{1,2})$. Finally, one recalls that the expressions for $\tilde{u}^r$, $\tilde{u}^d_{1,2}$, $\tilde{u}^{sd}_{1,2}$, and $\tilde{u}^i(Q_{1,2})$ contain quantities $R(\phi)$, L^{ew}, γ, $M^{eq}_{1,2}$ (or $\overline{M}^{eq}$), R^{eq}, D, L_p, D_p and α_p. In particular, $R(\phi)$ in $\tilde{u}^r$ is given by Equations (A-125) and (A-140) in Appendix III for the TE_z and TM_z cases, respectively. The L^{ew} and γ are given in Appendix III by Equations (A-123) and (A-124) respectively for the TE_z case; whereas, they are given by Equations (A-138) and (A-139) respectively for the TM_z case. The strengtn of the equivalent current $M^{eq}_{1,2}(\delta_{1,2})$ is given by Equations (A-145) and (A-152) for the TE_z and TM_z cases, respectively in Appendix IV. Also given in Appendix IV are the expressions for R^{eq}, L_p, D_p and α_p for the TE_z and TM_z cases, respectively; specifically, one is referred to Equations (A-143), (A-144b), (A-149), (A-151), (A-147), and (A-155) for these expressions. Also, the D appearing in $\tilde{u}^d_{1,2}$ and in $M^{eq}_{1,2}$ (of Equations (A-145) and (A-152)) is given by Equations (A-74) and (A-97) for the TE_z and TM_z cases, respectively in Appendix II.

Finally, one notes that the ray fields $\tilde{u}^d_{1,2}$ and $\tilde{u}^{sd}_{1,2}$ on the lit and shadow sides of the shadow boundary $SBQ_{1,2}$ are not valid within the transition region adjacent to $SBQ_{1,2}$. The angular extent of the transition region is $O[(ka)^{-1/3}]$ radians. Following a generalization of the analysis in [6] which is based on the results of Ivanov[7], one obtains the necessary modifications which constitute uniform approximations for the fields $\tilde{u}^d_1$ and $\tilde{u}^{sd}_1$ in the transition region by firstly replacing the expression in Equation (22) for $\tilde{u}^{sd}_1$ with

$$\tilde{u}_1^{sd}(P) \sim C_o\, M_1^{eq} \begin{Bmatrix} g(\xi_1) \\ -j\dfrac{\tilde{g}(\xi_1)}{m} \end{Bmatrix} e^{-jk\ell_1} \frac{e^{-jks_1}}{\sqrt{s_1}} \quad ; \text{ for} \begin{Bmatrix} TE_z \\ TM_z \end{Bmatrix} \text{case,} \qquad (24)$$

and by replacing the expression in Equations (18) or (20) for $\tilde{u}_1^d$ with

$$\tilde{u}_1^{d}(P) \sim C_o\, M_1^{eq} \begin{Bmatrix} g(\hat{\xi}_1)\, e^{-j\frac{\hat{\xi}_1^3}{3}} \\ -j\dfrac{\tilde{g}(\hat{\xi}_1)}{m}\, e^{-j\frac{\hat{\xi}_1^3}{3}} \end{Bmatrix} \frac{e^{-jks_1}}{\sqrt{s_1}} \quad ; \quad \text{for} \begin{Bmatrix} TE_z \\ TM_z \end{Bmatrix} \text{case.} \qquad (25)$$

Equation (24) for $\tilde{u}_1^{sd}$ is to be employed for P in the shadow zone of the transition region; whereas, Equation (25) for $\tilde{u}_1^{d}$ is to be employed for P in the lit zone of the transition region. The Fock functions $g(\cdot)$, and $\tilde{g}(\cdot)$ are defined in [6]; they are also defined and tabulated in [5].

$$\xi_1 = \frac{m\ell_1}{a} \quad ; \quad \hat{\xi} = -m \cos\left(\frac{\pi}{2} - \delta_1\right) , \quad \left(\delta_1 < \frac{\pi}{2} \text{ in transition region}\right) \qquad (26a,b)$$

and

$$m = \left(\frac{ka}{2}\right)^{1/3} . \qquad (27)$$

Although the above field expressions in Equations (24) and (25) are associated with the transition region adjacent to SBQ_1, similar expressions apply to the transition region adjacent to SBQ_2. It was mentioned previously that $M_{1,2}^{eq}(\delta_1)$ is inhomogeneous, i.e., it depends on the aspect ϕ via the angle $\delta_{1,2}$ (see Equation (19) for example); however, it is important to note that while $M_{1,2}^{eq}$ in Equations (18), (19), and (25) depend on $\delta_{1,2}$; the $M_{1,2}^{eq}$ in Equations (22) and (24) is evaluated at $\delta_{1,2} = 0$ as indicated in detail in Appendix IV.

III. NUMERICAL RESULTS AND DISCUSSION

Numerical results for the radiation patterns of the antenna configurations of Figures 1 and 2 are presented in this section; the patterns have been calculated via the GTD results which are developed for these configurations in Section II. The radiation patterns for the axial slot or TE_z case are presented for the planar and cylindrical configurations in Figures 9-15; whereas, those for the circumferential slot or TM_z case are presented in Figures 16-20. These patterns are normalized to 0 dB at their peak value.

The results of the GTD calculations are compared against corresponding results which are obtained via an independent calculation based on a combination of the method of moments (MM) and the GTD; the latter method abbreviated as MM-GTD as applied to the antenna configurations of Figures 1 and 2 is discussed in a separate report [8]. The MM-GTD is also an approximate method; however, it is expected to be slightly more accurate than the initial GTD analysis presented in this report. It is noted that in general, the results obtained by the present GTD analysis agree well with those obtained by the MM-GTD analysis of [8].

In general, one notes that increasing the size of the impedance patch increases the number of pattern ripples in the lit region (i.e., in the region of space where the slot is directly visible); whereas, increasing the size of the cylinder tends to decrease the level of the radiation pattern in the deep shadow region of the slot. Over the range of impedance values considered in the present calculations, one notes that increasing the value of the surface impedance for the TE_z case in general increases the size of the pattern ripple in the lit region; whereas, the reverse appears to be true for the TM_z case.

The high lobe structure caused by the use of the surface impedance patch is a direct consequence of a poor impedance match at the edges of the patch. This is harmful for the TE_z case but it is a disaster for the TM_z excitation. Tapering for impedance matching purpose has been used in the other report [8] but it would not be of any real import as it was used in so far as the TM_z geometry is concerned since the presence of the zero surface impedance would always cause a strong reflection. Consideration should be given to terminating the structure in an impedance surface whose value is chosen so that no surface wave exists. This should force the energy off the surface and in the desired direction with minimum back reflection as is the case in corrugated horn structures.

The GTD method presented in this report yields a simple and efficient procedure to analyze the radiation patterns of the antenna configurations in Figures 1 and 2; furthermore, due to the local nature of the GTD, it provides a physical insight into the radiation mechanisms involved. The numerical results indicate that this method indeed works well. However, some refinements and modifications of the present analysis are required to make the present GTD analysis useful and more accurate under general conditions. For example, it

would be worth investigating the following topics in this connection. It is of interest to investigate whether a more accurate representation for the fields on the impedance surface region would improve the GTD analysis for smaller size impedance patches, and even smaller size cylinders. In the planar case, one notes that the possibility of multiple surface wave reflection - diffraction exists, and this interaction could be quite important if the surface wave reflection coefficient at the ends of impedance patch is large. When interactions are important, it is important to have an accurate representation for the surface field which impinges on the ends of the impedance patch; otherwise, the errors could accumulate with the inclusion of each higher order multiple interaction. Furthermore, for the size of the impedance patches considered in the present calculations may not be long enough to assume that the space wave component of the field of a slot in an impedance surface is vanishingly small at the ends of the patch, hence some errors could result from not employing a more accurate representation for the field on the impedance surface in this case. One notes that only the surface wave mode or the Elliot type mode field is assumed to exist over the planar or curved impedance sections, respectively, in this study however this may be true only for large size impedance sections. Intimately tied in with this improved surface field calculation is the inclusion of the effects of the Watson type modes on the curved impedance section to obtain a better surface field representation in this case; however, since a calculation of the propagation constants of these Watson type modes could present some numerical problems for certain values of the surface impedance, an alternative surface field expression involving a modified Fock integral for the curved impedance surface should be investigated. Of course, one would have to look at ways to approximate this Fock type integral for the field on the curved impedance surface for ease of numerical computations. Furthermore, the inclusion of not only the Elliot mode, but also the Watson modes on the curved impedance patch leads to a more complicated analysis for the diffraction of the Watson modes from the ends of the impedance patch; in particular the analysis of this problem is more complicated within the transition regions adjacent to shadow boundaries SBQ_1 and SBQ_2 (see Figure 6), than that presented here for only the Elliot mode case. The diffraction effects of the Watson type modes are assumed to be negligible in the present analysis; the conditions under which this assumption is true needs to be more carefully investigated.

It would be interesting to study the transition region problem associated with the diffraction of the Watson type modes over a curved impedance patch, as it is the dominant effect within this transition region for curved impedance sections which do not support an Elliot type mode (e.g., a capacitive reactance surface in the axial slot or TE_z case). Some of these problems will be investigated in the future phases of this study.

These proposed modifications are expected to further improve the accuracy of the GTD calculations presented in this section, in addition to making the GTD method work under somewhat more general conditions which may be encountered in practical antenna problems of the type shown

in Figures 1 and 2. While the use of the MM-GTD method for analyzing these problems [8] is far more efficient than the conventional MM techniques, it is less efficient than the analysis based on just the GTD alone. At the present, the MM-GTD method is applicable under more general situations than those presently handled by the GTD, e.g., it is applicable to variable curvature cylinders and variable surface impedance cases; furthermore it is applicable to the cases in which the surface impedance does not support surface wave, or Elliot type modes. Some refinements are also required in the MM-GTD methods as pointed out in [8]; these refinements will also be studied in addition to the continuing GTD study of the antenna problems of Figures 1 and 2. In conclusion, the GTD method does show promise of being a useful method in analyzing the antenna problems of Figures 1 and 2.

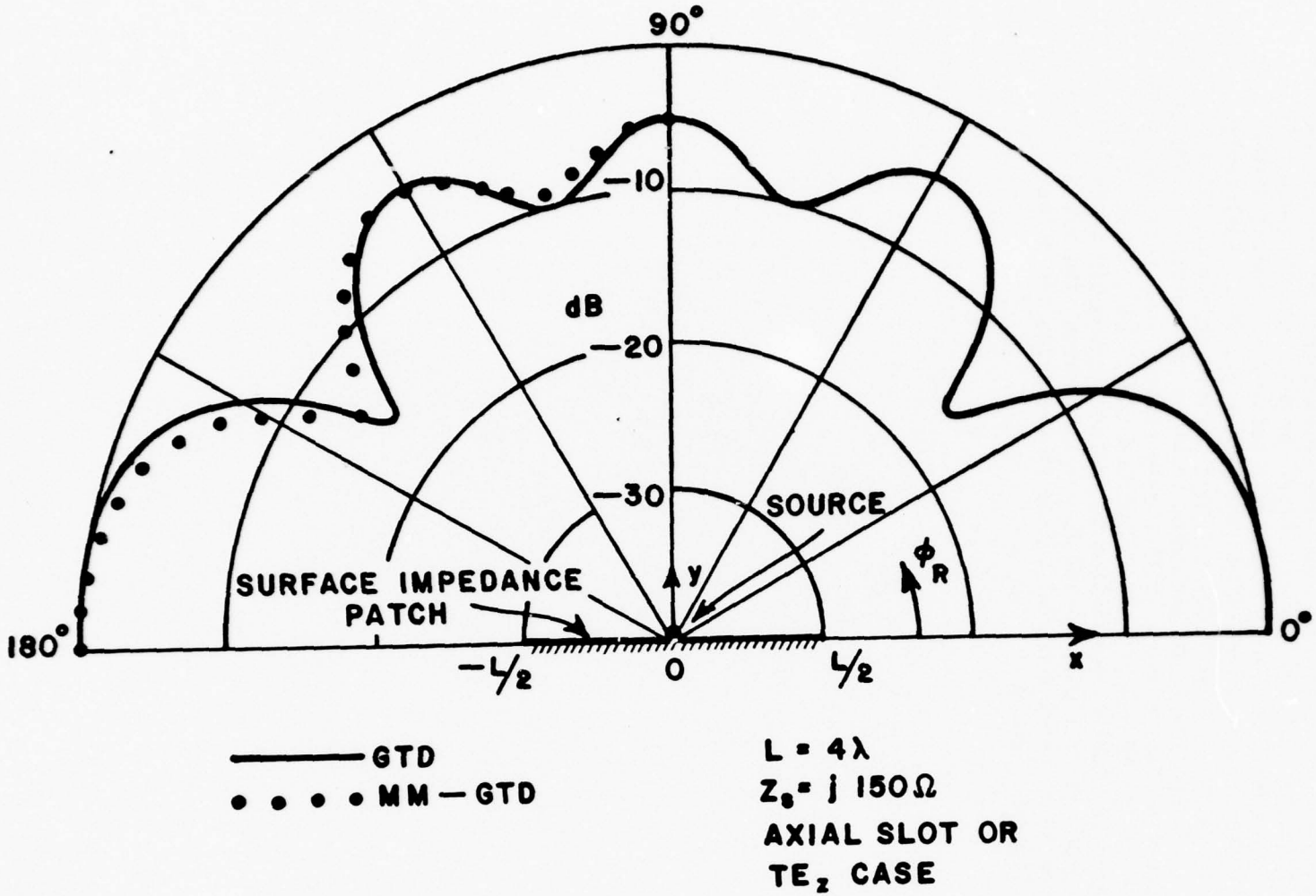

Figure 9. Radiation pattern of a magnetic line source on a perfectly-conducting planar surface which is covered with an impedance surface patch.

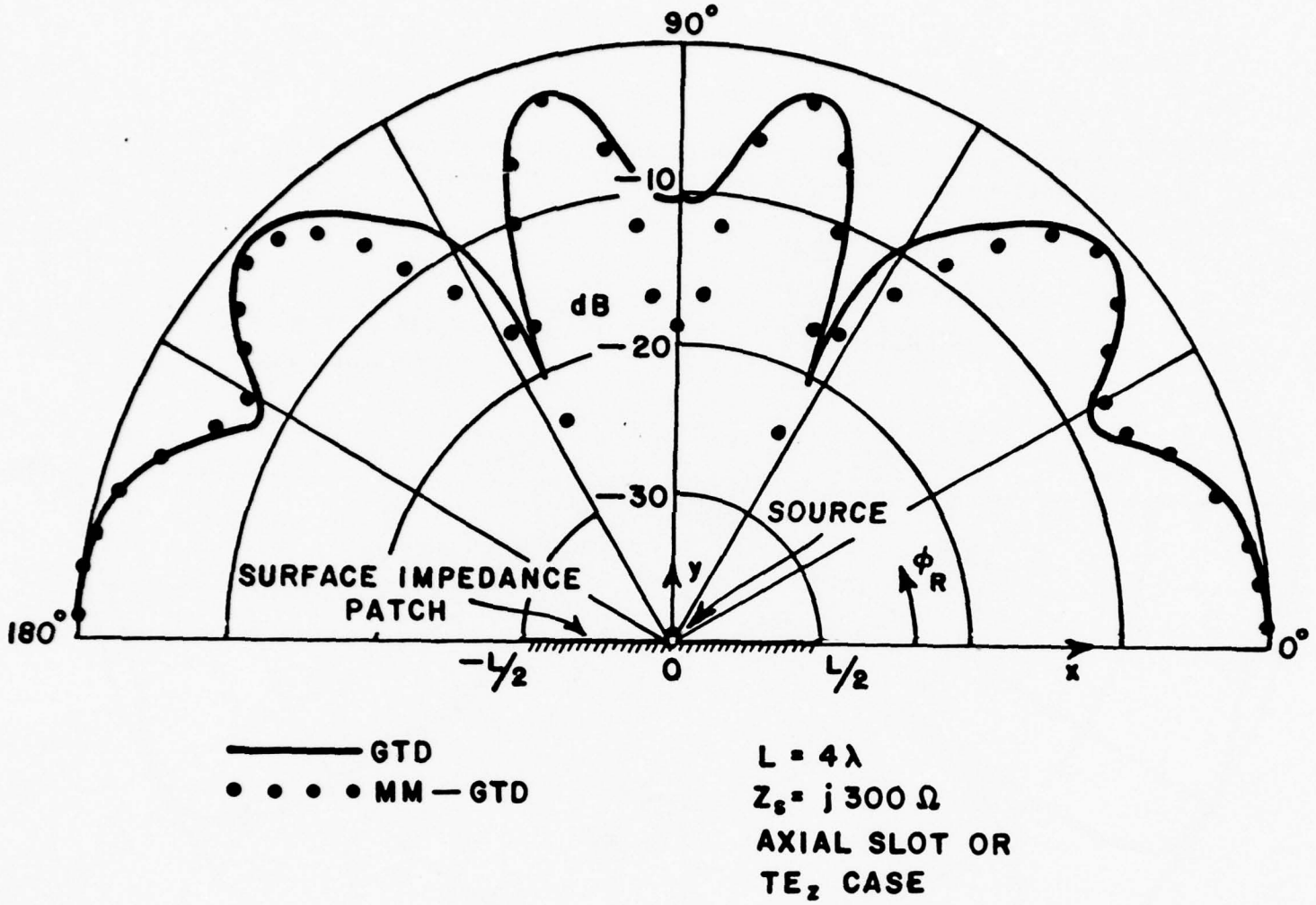

Figure 10. Radiation pattern of a magnetic line source on a perfectly-conducting planar surface which is covered with an impedance surface patch.

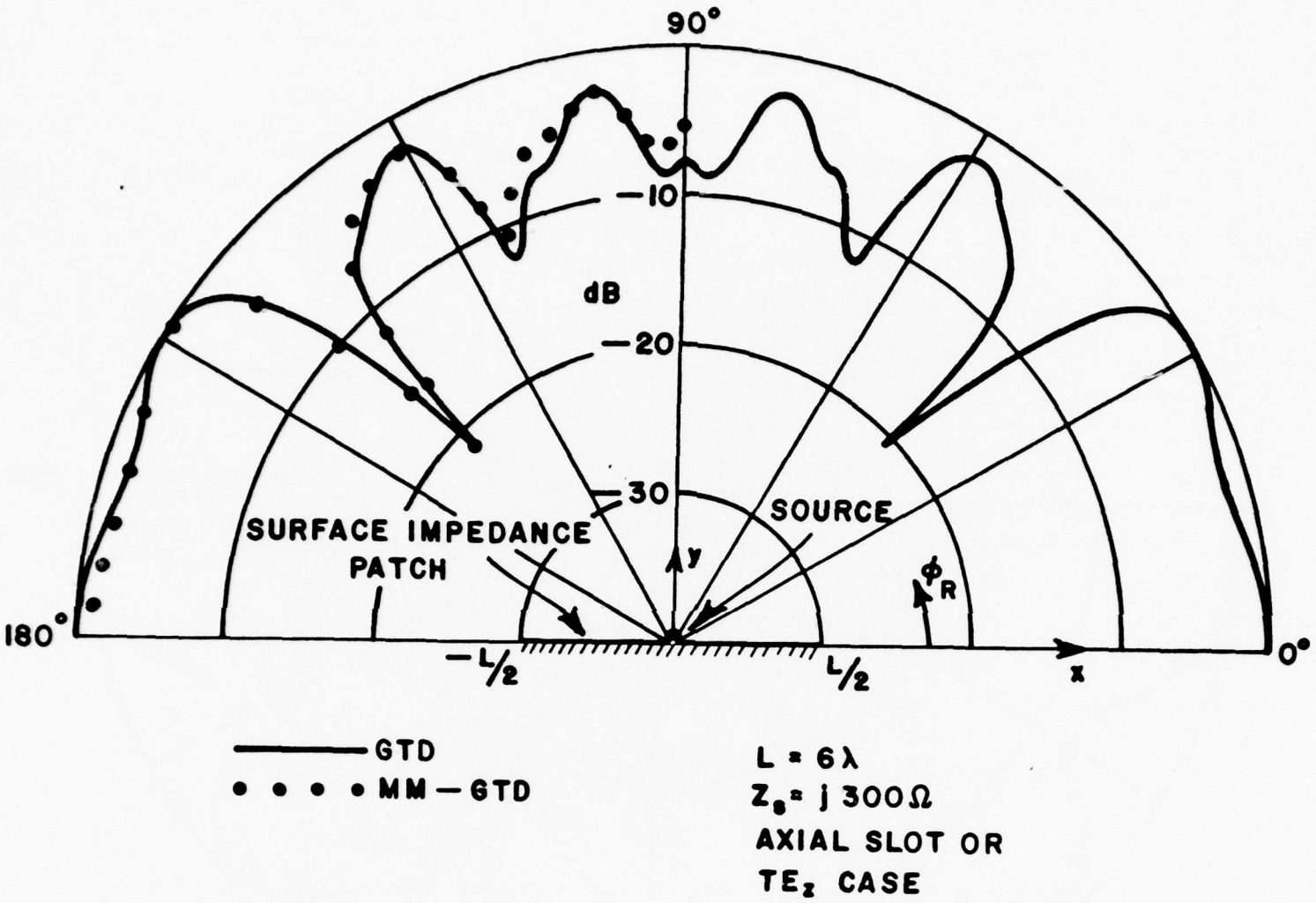

Figure 11. Radiation pattern of a magnetic line source on a perfectly-conducting planar surface which is covered with an impedance surface patch.

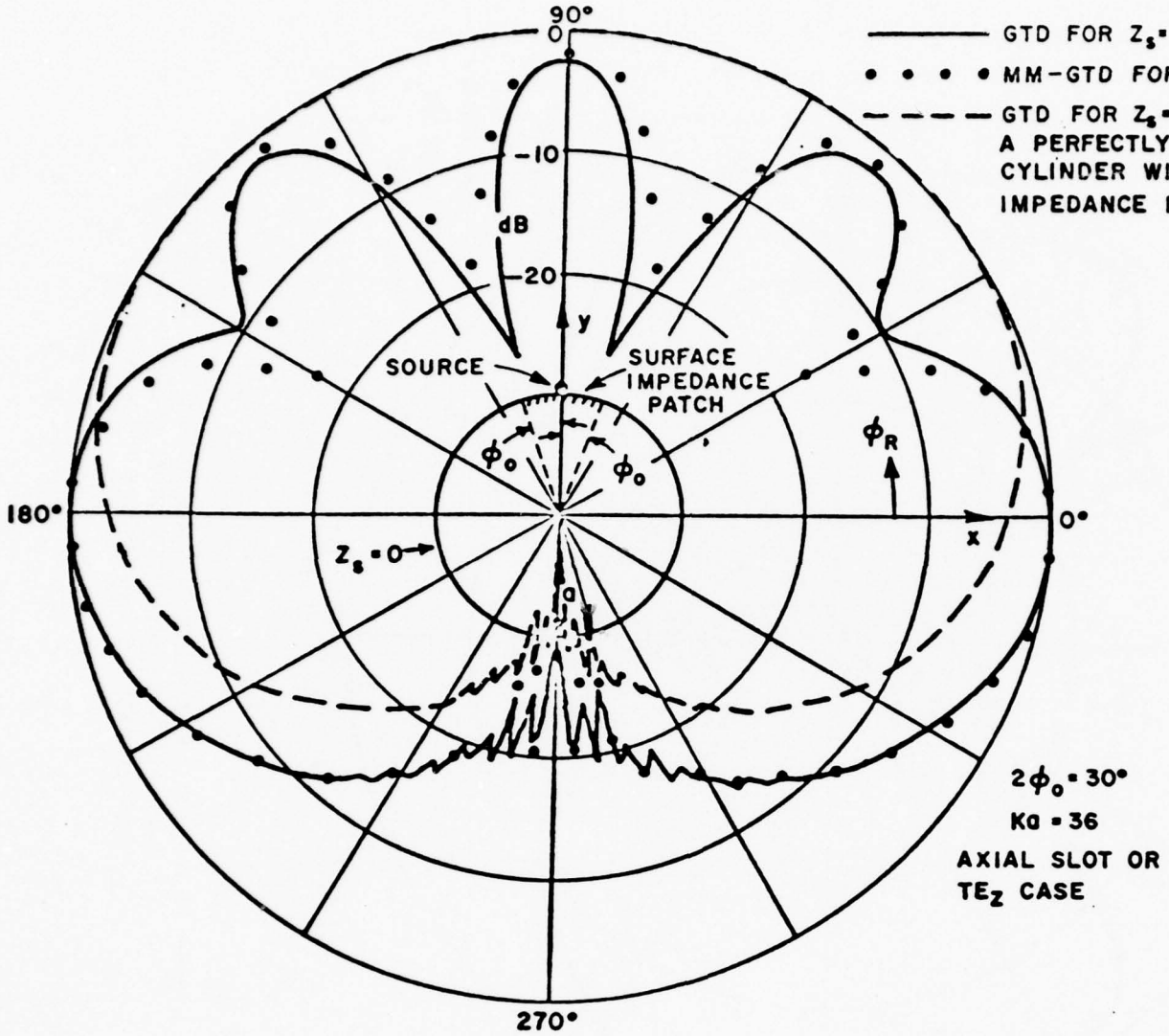

Figure 12. Radiation pattern of a magnetic line source on a perfectly-conducting circular cylinder which is covered with an impedance surface patch.

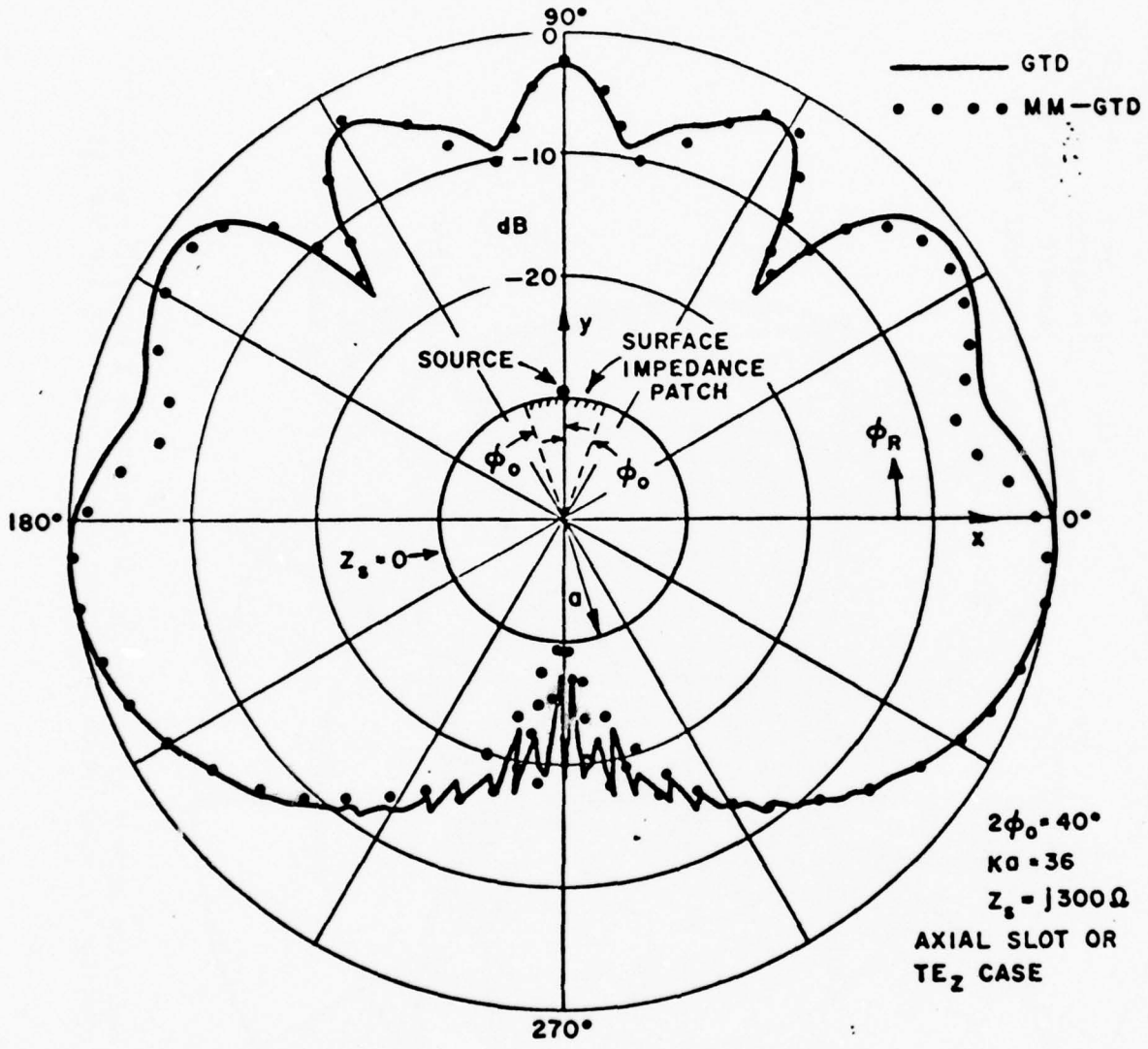

Figure 13. Radiation pattern of a magnetic line source on a perfectly-conducting circular cylinder which is covered with an impedance surface patch.

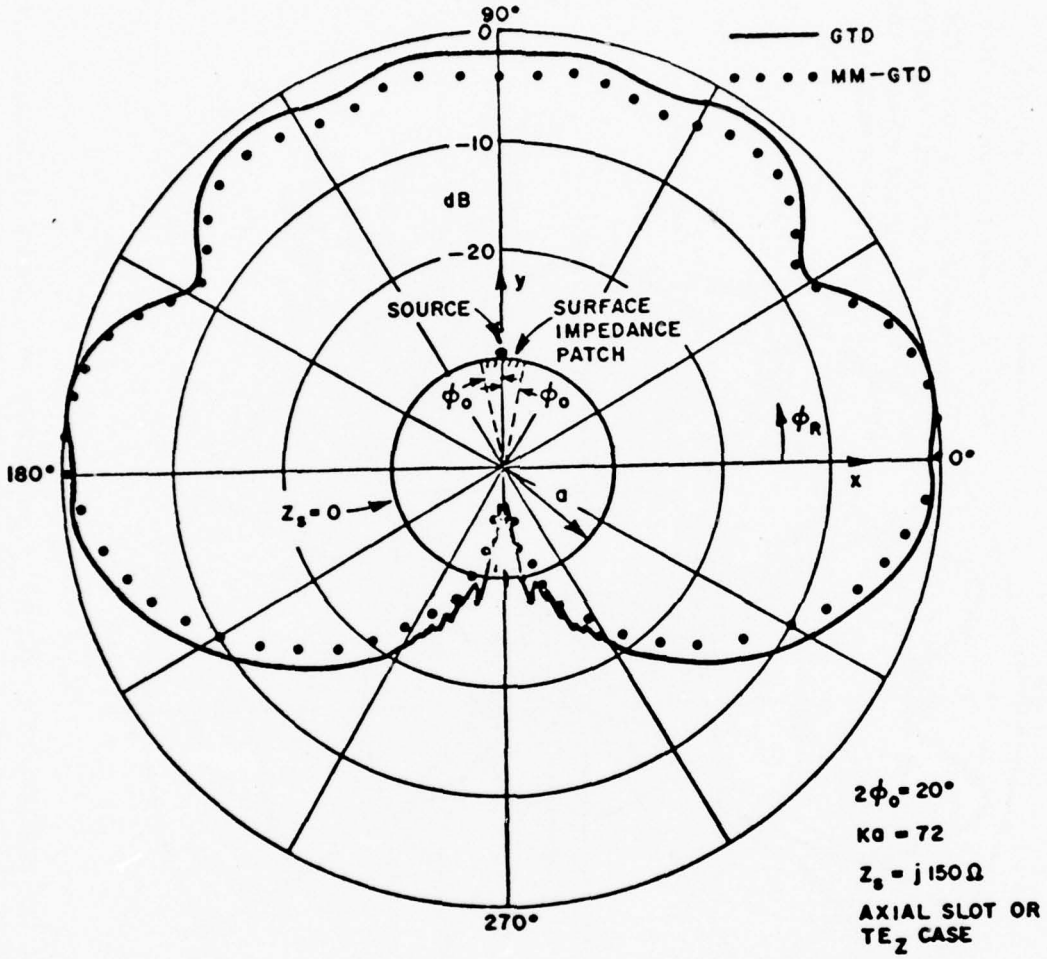

Figure 14. Radiation pattern of a magnetic line source on a perfectly-conducting circular cylinder which is covered with an impedance surface patch.

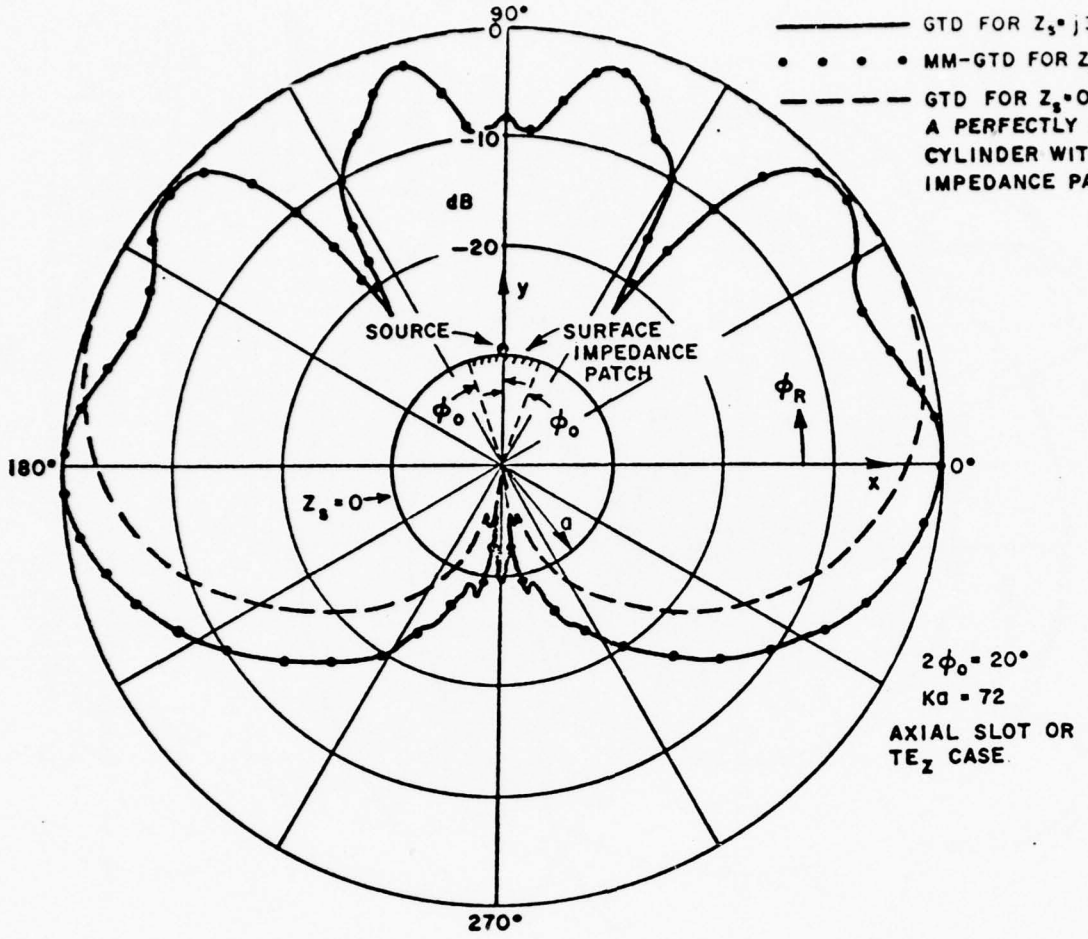

Figure 15. Radiation pattern of a magnetic line source on a perfectly-conducting circular cylinder which is covered with an impedance surface patch.

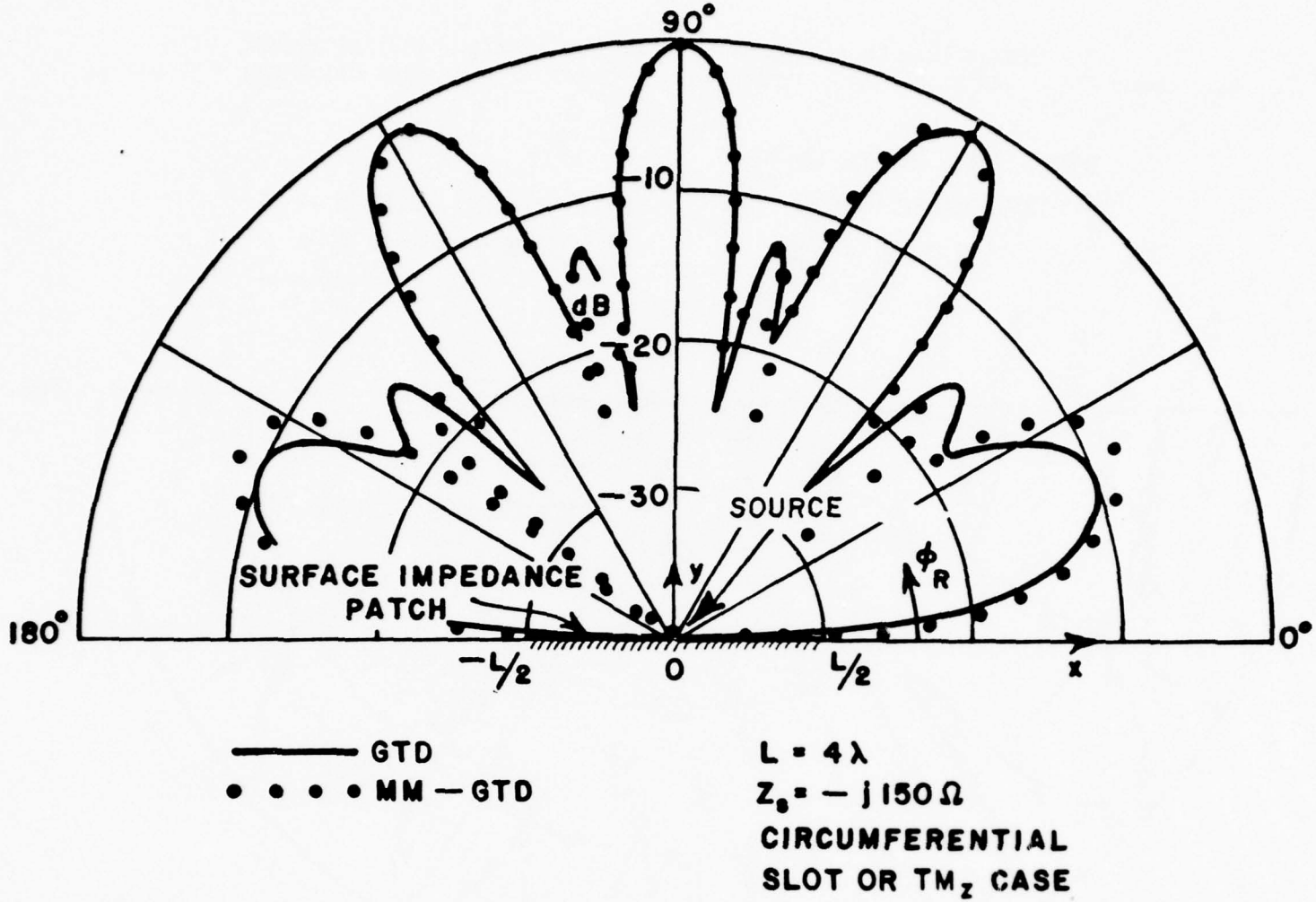

Figure 16. Radiation pattern of a magnetic line dipole source on a perfectly-conducting planar surface which is covered with an impedance surface patch.

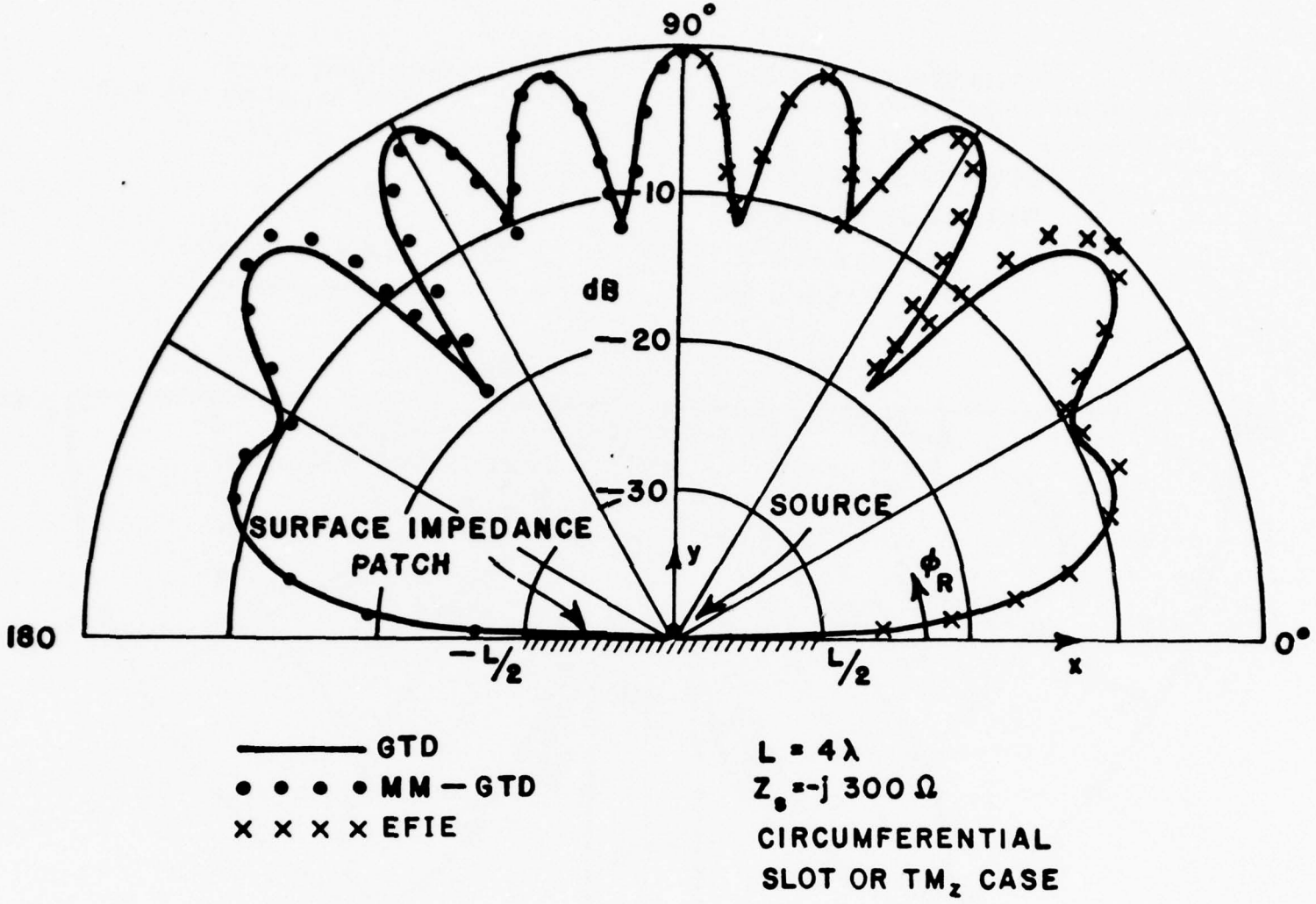

Figure 17. Radiation pattern of a magnetic line dipole source on a perfectly-conducting planar surface which is covered with an impedance surface patch.

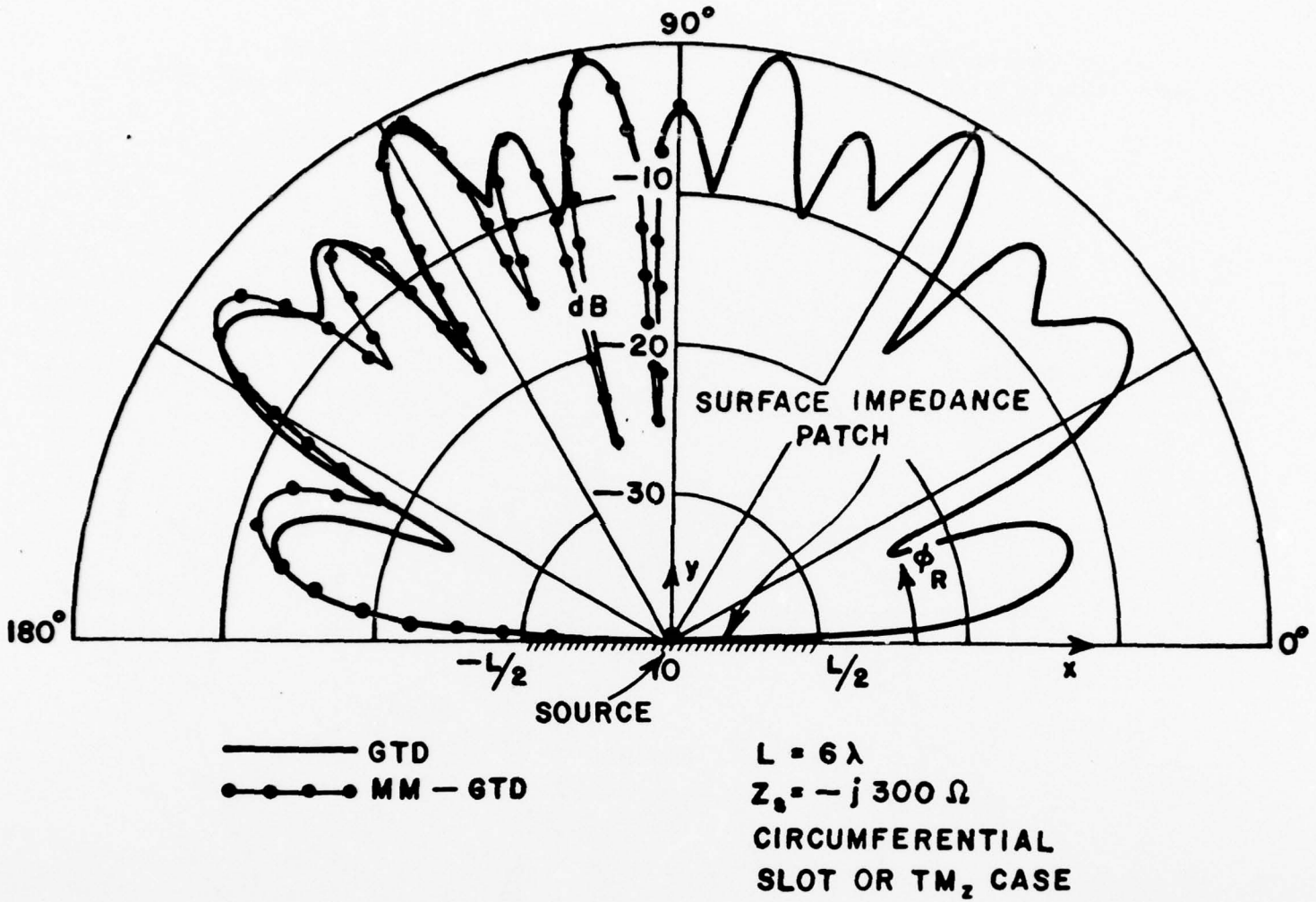

Figure 18. Radiation pattern of a magnetic line dipole source on a perfectly-conducting planar surface which is covered with an impedance surface patch.

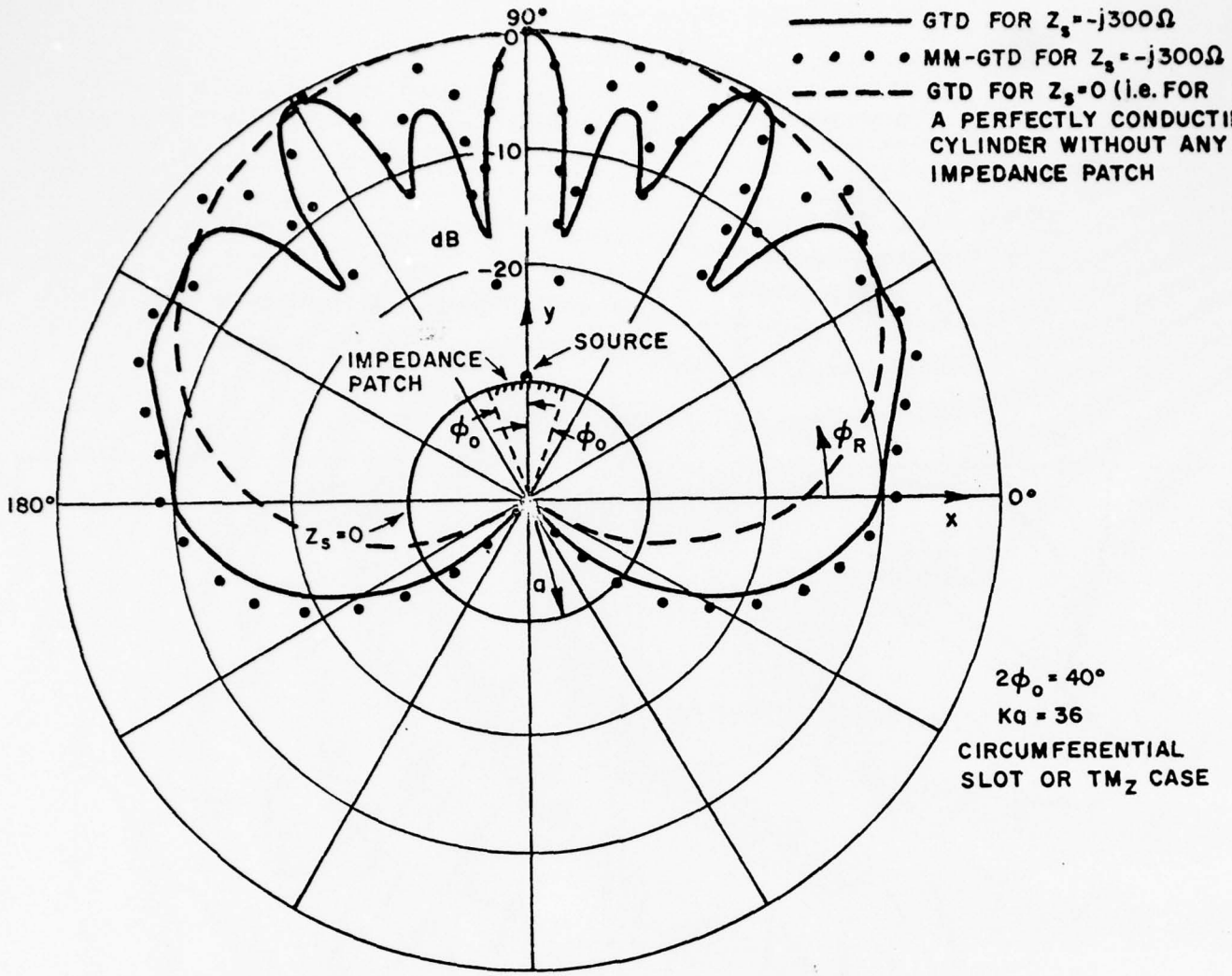

Figure 19. Radiation pattern of a magnetic line dipole source on a perfectly-conducting circular cylinder which is covered with an impedance surface patch.

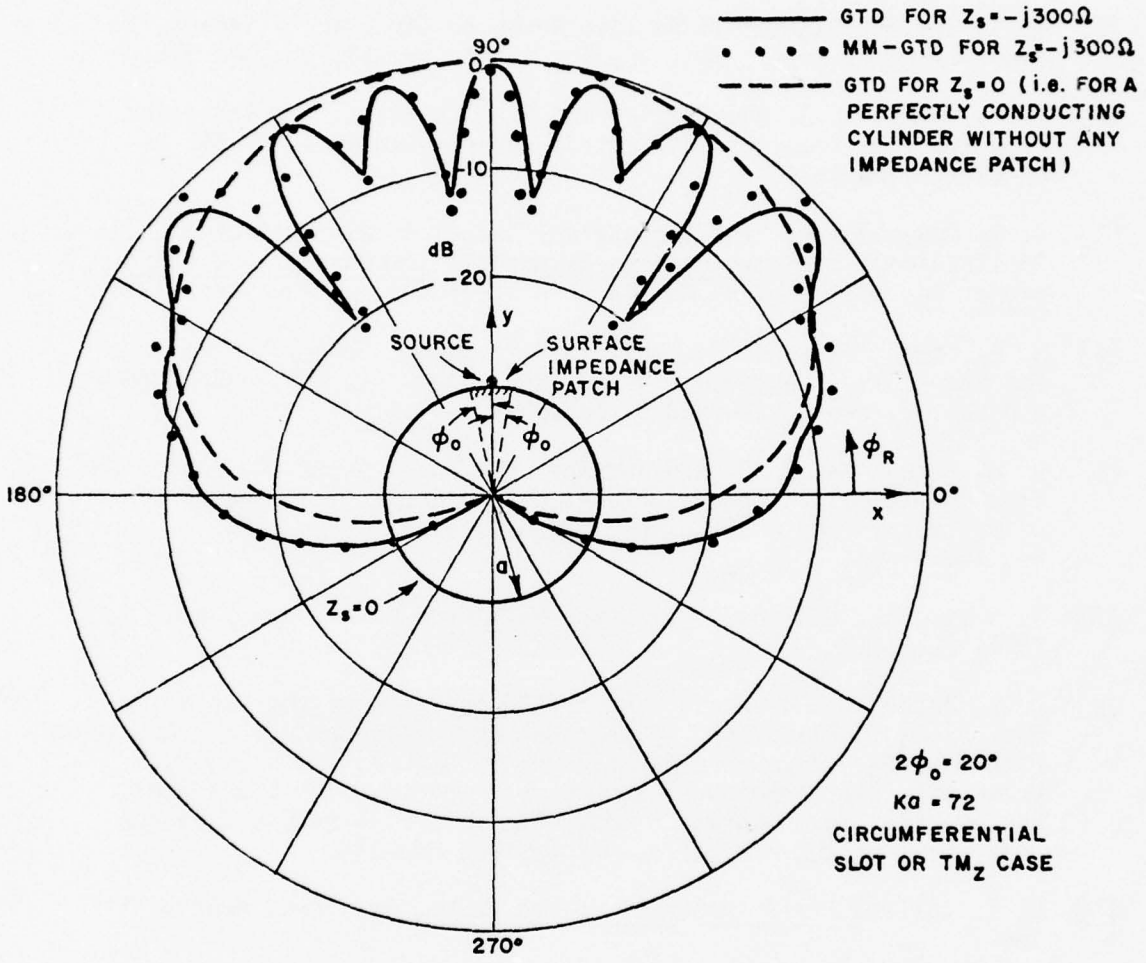

Figure 20. Radiation pattern of a magnetic line dipole source on a perfectly-conducting circular cylinder which is covered with an impedance surface patch.

REFERENCES

[1] J. B. Keller, "Geometrical Theory of Diffraction," Jour. Opt. Soc. Amer., Vol. 52, No. 2, February 1962, pp. 116-130.

[2] R. S. Elliot, "Azimuthal Surface Waves on Circular Cylinders," Jour. of Appl. Phys., Vol. 26, No. 4, April 1955, pp. 368-376.

[3] Y. M. Hwang, R. G. Kouyoumjian and P. H. Pathak, "The Radiation From Slots in Truncated Dielectric-covered Surfaces," NASA CR-2397, June 1974.

[4] R. G. Kouyoumjian, "The Geometrical Theory of Diffraction and Its Application," in Numerical and Asymptotic Techniques in Electromagnetics, edited by R. Mittra. Springer-Verlag, New York, 1975.

[5] N. A. Logan, "General Research in Diffraction Theory," Missiles and Space Div., Lockheed Aircraft Corp., Vol. 1, Rep. LMSD-288087 and Vol. 2, Rep. LMSD-288088, December 1959.

[6] P. H. Pathak and R. G. Kouyoumjian, "An Analysis of the Radiation from Apertures in Curved Surfaces by the Geometrical Theory of Diffraction," Proc. IEEE, Vol. 62, No. 11, November 1974, pp. 1438-1447.

[7] V. I. Ivanov, USSR Jour. of Comp. Math. and Math. Phys., Vol. 2, 1971, p. 216.

[8] P. H. Pathak and J. Huang, "An MM-GTD Analysis of the Radiation from Slots in Planar and Cylindrical Perfectly-Conducting Structures with a Surface Impedance Patch," Report 4396-1, The Ohio State University ElectroScience Laboratory, Department of Electrical Engineering; in preparation under Contract F19628-76-C-0154 for Department of the Air Force, Air Systems Command.

[9] R. E. Collin, Field Theory of Guided Waves, New York, McGraw-Hill, 1960.

[10] Collin and Zucker Eds., Antenna Theory, Pt. II, New York, McGraw-Hill, 1969.

[12] B. Noble, Methods Based on the Wiener-Hopf Technique, Pergamon Press, Oxford, 1958.

[13] R. Mittra and S. W. Lee, Analytical Techniques in the Theory of Guided Waves, Macmillan Co., New York, Collier-Macmillan Ltd., London, 1971.

[14] L. A. Weinstein, The Theory of Diffraction and the Factorization Method, the Golem Press, Boulder, Colorado, 1969.

APPENDIX I

AN ANALYSIS OF THE CANONICAL PROBLEM OF THE RADIATION FROM A LINE SOURCE ON AN INFINITE PLANAR IMPEDANCE SURFACE

The geometrical configuration of the problem is illustrated in Figure 4. A magnetic line source at 0 excites this configuration of interest. This line source is designated by $\overline{M}$, and it represents a $\hat{z}$-directed quantized, equivalent magnetic line source for the axial slot (or the TE_z) case; whereas, it represents an $\hat{x}$-directed quantized, equivalent magnetic line dipole source for the circumferential slot (or TM_z) case. The TE_z case is treated first; it is followed by a similar analysis for the TM_z case.

TE_z or the axial slot case

The magnetic line source $\overline{M}$ is specifically given by

$$\overline{M} = \hat{z}\, M\, \delta(x)\delta(y) \tag{A-1}$$

where the strength M is assumed known. The magnetic field radiated by this source in the presence of the infinite planar impedance surface is entirely $\hat{z}$-directed (hence the fields are TE_z type). Let this magnetic field be denoted by h_z. h_z satisfies the reduced, inhomogeneous wave equation, and the following boundary conditions.

$$(\nabla_t^2 + k^2)\, h_z = jkY_o\, M\, \delta(x)\delta(y-h)\ ;\quad h\to 0 \text{ and } y\geq 0;\ |x|<\infty. \tag{A-2}$$

$$\frac{\partial h_z}{\partial y} = jk\,\frac{Z_s}{Z_o}\, h_z \quad ,\ \text{at } y=0; \qquad |x|<\infty \text{ and } Z_s \text{ is the surface impedance value.} \tag{A-3}$$

One notes that Y_o = free space admittance and $Z_o = Y_o^{-1}$. ∇_t^2 is the two dimensional Laplacian operator. Also, h_z satisfies the radiation condition as $\rho\to\infty$. The solution to a similar problem is discussed elsewhere [9,10]; however, a method of solution based on Green's functions is presented here for the sake of completeness. Only the significant steps in the analysis will be indicated for the sake of brevity. Let g_m denote a Green's function which satisfies the following equations:

$$(\nabla_t'^2 + k^2) g_m(\overline{\rho}'|\overline{\rho}) = -\,\delta(x'-x)\delta(y'-y);\ (y,y')\geq 0,\ |x,x'|<\infty, \tag{A-4}$$

where $\nabla_t'^2$ is the 2-D Laplacian in the primed coordinate system (x',y'). $\bar{\rho} = x\hat{x} + y\hat{y}$; whereas $\bar{\rho}' = x'\hat{x} + y'\hat{y}$.

$$\frac{\partial g_m}{\partial y'} = jk \frac{Z_s}{Z_o} g_m; \quad \text{at } y'=0, \ |x'|<\infty \ . \tag{A-5}$$

Also, g_m satisfies the radiation condition. Utilizing the two-dimensional Green's theorem and the reciprocity condition $g_m(\bar{\rho}'|\bar{\rho}) = g_m(\bar{\rho}|\bar{\rho}')$, one obtains

$$h_z(x,y) = - jkY_o \, M \, g(x,y|0,h); \quad h\to 0. \tag{A-6}$$

Using the procedure for constructing higher dimensional Green's function as in [10], one obtains

$$g_m = - \frac{1}{2\pi j} \oint_{C_x} g_{mx}(x|x') \cdot g_{my}(y|y') \, d\lambda_x \tag{A-7a}$$

where the one dimensional Green's functions g_{mx} and g_{my} satisfy the following differential equations and boundary conditions:

$$\left(\frac{\partial^2}{\partial x^2} + \lambda_x\right) g_{mx} = - \delta(x-x'); \qquad \left(\frac{\partial^2}{\partial y^2} + \lambda_y\right) g_{my} = - \delta(y-y') \tag{A-7b;A-7c}$$

g_{mx} and g_{my} satisfy the radiation condition at $\rho\to\infty$; $\quad \frac{\partial}{\partial y} g_{my} = jk \frac{Z_s}{Z_o} g_{my}$ at $y=0$. (A-7d;A-7e)

In addition

$$\lambda_x + \lambda_y = k^2. \tag{A-7f}$$

The contour C_x encloses only the singularities of g_{mx} in the complex λ_x plane. g_{mx} and g_{my} are found to be

$$g_{mx} = \frac{e^{-j\sqrt{\lambda_x}|x-x'|}}{2j\sqrt{\lambda_x}} \ ; \quad g_{my} = \frac{e^{-j\sqrt{\lambda_y}(y-h)} + R_h \, e^{-j\sqrt{\lambda_y}(y+h)}}{2j\sqrt{\lambda_y}} \tag{A-7g;A-7h}$$

in which $y > h \to 0$. The contour c_x runs in the counter-clockwise sense around the branch cut singularity of g_{mx} along $\mathrm{Re}\lambda_x \geq 0$. Introducing the transformation $k_x^2 = \lambda_x$, one obtains

$$g_m(x,y|o,h) = \frac{1}{2\pi j}\int_{-\infty-j\varepsilon}^{\infty+j\varepsilon} dk_x \frac{e^{-j\sqrt{\lambda_y}(y-h)} + R_h e^{-j\sqrt{\lambda_y}(y+h)}}{2\sqrt{\lambda_y}} e^{-jk_x|x|} \tag{A-8}$$

in which $x'=0$, $y'=h$, and $y>h\to 0$. Also,

$$R_h = \frac{\sqrt{\lambda_y} - k\, Z_s/Z_o}{\sqrt{\lambda_y} + k\, Z_s/Z_o} = \frac{\sqrt{k^2-k_x^2} - k\, Z_s/Z_o}{\sqrt{k^2-k_x^2} + k\, Z_s/Z_o} \quad . \tag{A-9}$$

The contour of integration in Equation (A-8) is illustrated in Figure A-1. The branch cuts in Figure A-1 are chosen such that $\mathrm{Im}\sqrt{\lambda_y}<0$. It is convenient for subsequent evaluation of Equation (A-8) to introduce further transformations

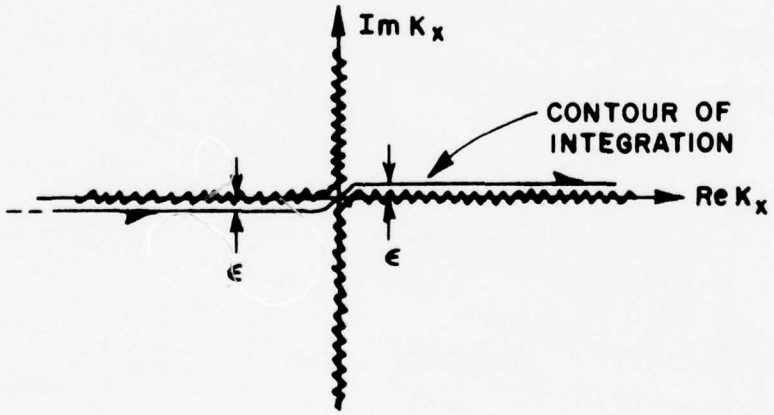

Figure A-1. Contour of integration in the complex k_x plane.

$$x = \rho\cos\phi \quad ; \quad y = \rho\sin\phi \quad , \tag{A-10}$$

and

$$k_x = k\cos\xi \quad ; \sqrt{\lambda_y} = \sqrt{k^2-k_x^2} = +\, k\sin\xi \equiv k_y \tag{A-11}$$

The Green's function g_m of Equation (A-8) is now expressed in the complex ξ plane as

$$g_m(x,y|o,h) = -\frac{1}{4\pi j}\int_C d\xi \left[e^{-jk\rho_1\cos(\phi-\xi)} + R_h(\xi)e^{-jk\rho_2\cos(\phi-\xi)}\right] \qquad (A\text{-}12)$$

where

$$y \mp h \equiv \rho_{1,2}\sin\phi \; ; \quad \text{and the corresponding } |x| \equiv \rho_{1,2}\cos\phi. \qquad (A\text{-}13a;A\text{-}13b)$$

One notes that $\rho_{1,2} \to \rho$ as $h \to 0$. Also,

$$R_h(\xi) = \frac{\sin\xi - Z_s/Z_o}{\sin\xi + Z_s/Z_o} \quad . \qquad (A\text{-}14)$$

The contour of integration c is indicated in Figure A-2. The integral in Equation (A-12) may be evaluated for large $k\rho_{1,2}$ via the method of steepest descent. Thus, the contour c is deformed into the steepest descent path SDP through the saddle point.

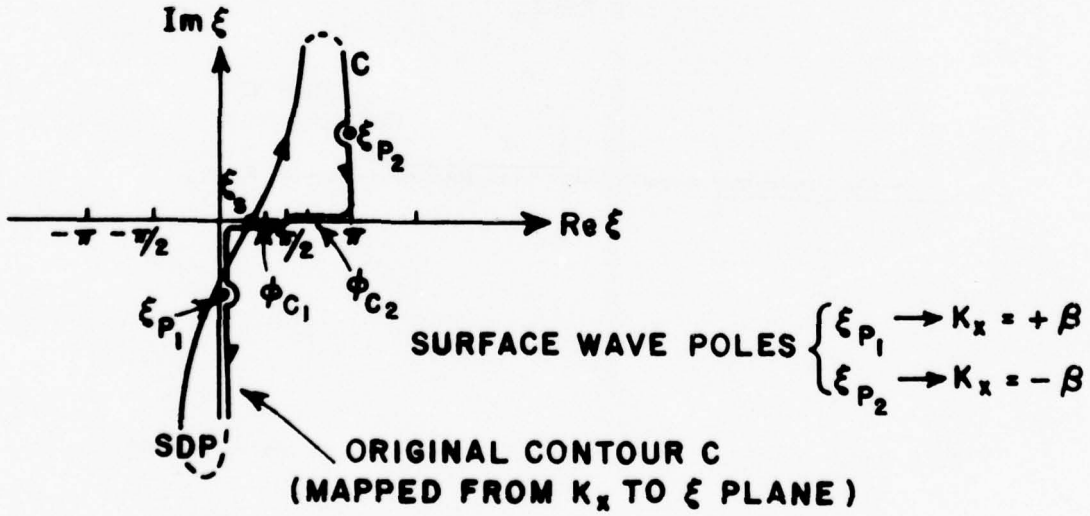

Figure A-2. Contour of integration in the ξ plane.

$$\xi = \xi_s = \phi \text{ (at the saddle point)}; \quad 0<\xi<\pi/2 \text{ if } 0<\phi<\pi/2. \tag{A-15}$$

The case $0<\phi<\pi/2$ is treated here. (A separate analysis for $\pi<\phi<\pi/2$ is not required since the results for this case may be obtained from those for $0<\phi<\pi/2$ by invoking symmetry.) In deforming the contour c into SDP, the poles of $R_h(\xi)$ may be crossed, hence, their residue contribution must be taken into account. The poles of $R_h(\xi)$ occur at

$$\sin \xi_p = - Z_s/Z_o \quad ; \quad \text{such poles certainly exist if } Z_s \text{ is chosen to be } jX_L \text{ where } X_L>0 \text{ (i.e., } Z_s \text{ is an inductive reactance).} \tag{A-16}$$

$$\xi_{P_1} = \sin^{-1} (-j\, X_L/Z_o) \text{ at the pole } \xi=\xi_{P1} \text{ for } x>0 \tag{A-17a}$$

and

$$\xi_{P_2} = \pi + \sin^{-1} (j\, X_L/Z_o) \text{ at the pole } \xi=\xi_{P2} \text{ for } x<0. \tag{A-17b}$$

Let

$$k \cos \xi_{P1} = \beta \quad ; \quad k \cos \xi_{P2} = - \beta \,, \tag{A-18a;A-18b}$$

where

$$\beta \equiv k\sqrt{1 + (X_L/Z_o)^2} \quad , \text{ with } Z_s = jX_L (X_L>0). \tag{A-19}$$

Finally, a saddle point evaluation of Equation (A-12) yields the following for pole not close to the saddle point.

$$g_m \sim -j\sqrt{\frac{j}{8\pi k}} \cdot \frac{2 \sin\phi}{\sin\phi + Z_s/Z_o} \frac{e^{-jk\rho}}{\sqrt{\rho}} - j \frac{\alpha}{\beta} e^{-\alpha y - j\beta|x|} U(\phi_{c1}-\phi)$$

$$\text{for } 0\leq\phi\leq\pi/2 \text{ and } h=0. \tag{A-20}$$

$$\alpha^2 \equiv \beta^2 - k^2, \ (\beta>k), \text{ and } \beta \text{ is defined in Equation (A-19).} \tag{A-21}$$

Also, $\mathbf{U}$ in Equation (A-20) denotes the Heaviside step function which is unity for $\phi<\phi_{cl}$; whereas it is zero for $\phi>\phi_{cl}$. The angle ϕ_{cl} is illustrated in Figure A-2. The first term on the RHS of Equation (A-20) is the so-called space wave contribution which vanishes along the impedance boundary (at $\phi=0, \pi$); whereas, the second term is the surface wave mode field which exists when $Z_s = j\ X_L (X_L>0)$. One may now find h_z in terms of Equation (A-6) and (A-20) to be

$$h_z(x,y) \sim u^r + u^i \tag{A-22}$$

where

$$u^r = c_o\ M\ R(\phi)\ \frac{e^{-jk\rho}}{\sqrt{\rho}} \tag{A-23}$$

and

$$u^i\Big|_{y=0} = c_o\ M\ L^{sw}\ e^{-j\beta|x|} \quad ; \quad |x|<\infty \ . \tag{A-24}$$

It is easily verified that if

$$c_o \equiv -\sqrt{\frac{jk}{8\pi}}\ Y_o \ , \tag{A-25}$$

then

$$R(\phi) = \frac{2\sin\phi}{\sin\phi + Z_s/Z_o} = \frac{2\sin\phi}{\sin\phi + j\alpha/k} \quad ; \quad \begin{array}{l} Z_s = j\ X_L \\ \text{and } \alpha/k = X_L/Z_o \end{array} \tag{A-26}$$

and

$$L^{sw} = -\sqrt{8\pi jk}\ \frac{j\alpha}{\beta} \tag{A-27}$$

where α and β are given in terms of the inductive reactance $Z_s = j\ X_L$ $(X_L>0)$ in Equation (A-19) and Equation (A-21).

TM_z or the circumferential slot case

The magnetic line source $\overline{M}$ at 0 in this case is a magnetic line dipole given by

$$\overline{M} = \hat{x}\, M\, \delta(x)\delta(y) \quad , \tag{A-28}$$

where the amplitude M is a known quantity. The electric field radiated by this source is entirely $\hat{z}$-directed (hence, the fields are TM_z type). Let this electric field be denoted by e_z. Then

$$(\nabla_t^2 + k^2)f = -\, M\, \delta(x)\delta(y-h) \quad ; \quad y \geq 0;\ |x|<\infty \text{ and } h \to 0 \tag{A-29}$$

where

$$e_z = -\frac{\partial f}{\partial y} \quad ; \quad e_z\, \hat{z} = -\, \nabla x(\hat{x}f) \tag{A-30}$$

and

$\hat{x}f$ is the electric vector potential.

The impedance boundary condition $e_z\, \hat{z} = \hat{y} \times Z_s\, \overline{h}_{tan}$ at $y=0$ where $\overline{h}_{tan}$ is the tangential magnetic field at $y=0$ corresponding to e_z implies that

$$\frac{\partial^2 f}{\partial y^2} = jk\, \frac{Z_o}{Z_s}\, \frac{\partial f}{\partial y} \qquad \text{at } y=0, \quad |x|<\infty \quad . \tag{A-31}$$

Let g_e be a Green's function which satisfies

$$(\nabla_t'^2 + k^2)g_e(\overline{\rho}'|\overline{\rho}) = -\, \delta(x'-x)\delta(y'-y) \quad ; \quad \begin{matrix} y \geq 0; |x|<\infty \\ y' \geq 0; |x'|<\infty \end{matrix} \tag{A-32}$$

$$\frac{\partial^2 g_e}{\partial y'^2} = jk\, \frac{Z_o}{Z_s}\, \frac{\partial g_e}{\partial y'} \quad \text{at } y'=0; \quad |x'|<\infty \quad . \tag{A-33}$$

The above Equation (A-33) could be simplified to $\frac{\partial g_e}{\partial y'} = jk\, \frac{Z_o}{Z_s}\, g_e$ at $y'=0$ by integrating with respect to y' and requiring that g_e and $\frac{\partial g_e}{\partial y'}$ satisfy the radiation condition. One may show that

$$f = M\, g_e(\bar{\rho}|\bar{\rho}') = M\, g_e(x,y|o,h),\ h\to 0. \tag{A-34}$$

In obtaining Equation (A-34), use is made of the fact that e_z, and f satisfy the radiation condition; also, g_e is chosen to satisfy the radiation condition. Following the procedure outlined for the construction of g_m in the TE_z case, one obtains

$$g_e(x,y|o,h) = \frac{1}{2\pi}\int_{-\infty-j\varepsilon}^{\infty+j\varepsilon} dk_x\, e^{-jk_x|x|}\left[\frac{e^{-j\gamma(y-h)}+R_s e^{-j\gamma(y+h)}}{2j\gamma}\right];\ \begin{matrix} y>h \\ h\to 0, \end{matrix} \tag{A-35}$$

where

$$\gamma = \sqrt{k^2-k_x^2} = \sqrt{\lambda_y}\ ; \qquad R_s = -\frac{\gamma - k\, Z_o/Z_s}{\gamma + k\, Z_o/Z_s}\ . \tag{A-36a;A-36b}$$

The contour of integration in Equation (A-35) is the same as in Figure A-1. Transforming the above integral into the contour integral over c in the complex ξ-plane of Figure A-2 via Equations (A-10) and (A-11), one obtains

$$e_z(x,y) = -M\frac{\partial}{\partial y} g_e(x,y|o,h) = -\frac{M}{4\pi}\int_c d\xi\, k\sin\xi\left[e^{-jk\rho_1\cos(\phi-\xi)} + R_s e^{-jk\rho_2\cos(\phi-\xi)}\right] \tag{A-37}$$

where $\rho_{1,2}$ are defined in Equations (A-13a;A-13b), and

$$R_s(\xi) = -\frac{\sin\xi - Z_o/Z_s}{\sin\xi + Z_o/Z_s}\ . \tag{A-38}$$

One notes that $R_s(\xi)$ can certainly have a pole when $Z_s = -jX_c$ ($X_c>0$); i.e., when Z_s is a capacitive reactance. Then, evaluating Equation (A-37) by the saddle point method while taken into consideration the residue at the pole of $R_s(\xi)$ when deforming c into SDP yields the following result for pole not close to the saddle point, and for $y\to 0$ (i.e., $\rho_{1,2}\to\rho$)

$$e_z(x,y) \sim - jkM \frac{2j\alpha/k}{\sin\phi+j\alpha/k} \sin\phi \left(-j\sqrt{\frac{j}{8\pi k}} \right) \frac{e^{-jk\rho}}{\sqrt{\rho}} -$$

$$- jkM \frac{\alpha^2}{\beta} e^{-\alpha y - j\beta|x|} U(\phi_{cl}-\phi); \quad 0 \leq \phi \leq \pi/2. \qquad \text{(A-39)}$$

The results for $\pi \leq \phi \leq \pi/2$ are directly obtained from the results for $0 \leq \phi \leq \pi/2$ above by invoking symmetry. One notes that α and β in Equation (A-39) are defined as

$$\beta^2 = \alpha^2 + k^2 \ (\beta > k); \qquad \alpha = kZ_o/X_c = -jk\, Z_o/Z_s \ (\text{with } Z_s = -jX_c)$$

(A-40a;A-40b)

in which $Z_s = - jX_c (X_c > 0)$ implies capacitive reactance as indicated earlier. One may rewrite Equation (A-39) as

$$e_z(P) \sim u^r + u^i \qquad \text{(A-41)}$$

where

$$u^r = c_o M R(\phi) \frac{e^{-jk\rho}}{\sqrt{\rho}} \qquad = \text{space wave} \qquad \text{(A-42)}$$

and

$$u^i\Big|_{y=0} = c_o M L^{sw} e^{-j\beta|x|} = \text{surface wave mode field.} \qquad \text{(A-43)}$$

If c_o is defined as

$$c_o = - \sqrt{\frac{jk}{8\pi}} \ , \qquad \text{(A-44)}$$

then

$$R(\phi) = \frac{(2\sin\phi)(Z_o/Z_s)}{\sin\phi + Z_o/Z_s} = \frac{(2\sin\phi)(j\alpha/k)}{\sin\phi + j\alpha/k} \qquad \text{(A-45)}$$

and

$$L^{sw} = \sqrt{8\pi jk} \ \frac{\alpha^2}{\beta} \qquad \text{(A-46)}$$

in which α and β are as defined in Equations (A-40a;A-40b), with $Z_s = - jX_c \ (X_c > 0)$.

APPENDIX II

AN ANALYSIS OF THE CANONICAL PROBLEM OF SURFACE WAVE DIFFRACTION BY A PLANAR, TWO PART IMPEDANCE SURFACE

The geometrical configuration of this canonical problem is illustrated in Figure 5. The incident field, u^i is a bound surface wave mode which propagates along the surface impedance boundary ($y=0$, $x<0$); and, it produces the reflected surface wave, and diffracted fields u^{rsw} and u^d, respectively upon striking the discontinuity in surface impedance at ($x=0$; $y=0$). One requires that the surface impedance be purely inductive in the TE_z case; whereas, it be purely capacitive in the TM_z case (to support the surface wave mode). In the TE_z case, the magnetic field is entirely $\hat{z}$-directed; whereas, in the TM_z case, the electric field is entirely $\hat{z}$-directed. Let

$$u^i \equiv \begin{Bmatrix} H_z^i \\ E_z^i \end{Bmatrix} \; ; \quad u^{rsw} \equiv \begin{Bmatrix} H_z^{rsw} \\ E_z^{rsw} \end{Bmatrix} \; ; \quad u^d \equiv \begin{Bmatrix} H_z^d \\ E_z^d \end{Bmatrix} \; ; \quad \text{for} \quad \begin{Bmatrix} TE_z \\ TM_z \end{Bmatrix} \text{ case,} \tag{A-47a;A-47b;A-47c}$$

where E_z and H_z refer to the $\hat{z}$-directed electric and magnetic field intensities in the TM_z and TE_z cases, respectively; also, the superscripts i, rsw and d in (A-47a;A-47b;A-47c) stand for incident, reflected and diffracted wave components, respectively. The incident field $\begin{Bmatrix} E_z^i \\ H_z^i \end{Bmatrix}$ constitutes a known excitation, and the fields $\begin{Bmatrix} E_z^d \\ H_z^d \end{Bmatrix}$ and $\begin{Bmatrix} E_z^{rsw} \\ H_z^{rsw} \end{Bmatrix}$ can be found via the Wiener-Hopf technique for solving the two part boundary value problem of Figure 5. The TE_z solution will be briefly outlined first; and a similar outline will follow for the TM_z case.

TE_z case

The excitation H_z^i has the form

$$H_z^i = e^{-\alpha y} e^{+i\beta x} \quad ; \quad |x| \leq \infty \tag{A-48}$$

in which it is assumed that H_z^i exists even for $x>0$.

$$\beta = k\sqrt{1 - \left(\frac{Z_s}{Z_o}\right)^2} \quad ; \qquad \alpha^2 = \beta^2 - k^2, \tag{A-49a;A-49b}$$

as in Equations (A-19) and (A-21) for the TE_z case with $Z_s = jX_L (X_L > 0)$ corresponding to inductive reactance. In the following analysis an $e^{-i\omega t}$ time convention will be employed for the sake of convenience in using the Wiener Hopf notation; however, a complex conjugate of the final results will yield back the $e^{j\omega t}$ time convention. The quantity $i = \sqrt{-1}$ instead of $j = \sqrt{-1}$ will be employed to distinguish between the two time conventions. Let H_z^s denote the scattered field, then the total field, $H_z = H_z^i + H_z^s$. The total field H_z satisfies

$$(\nabla_t^2 + k^2) H_z = 0; \qquad \text{for } y \geq 0, \quad |x| < \infty , \tag{A-50}$$

$$\frac{\partial H_z}{\partial y} = - ik \frac{Z_s}{Z_o} H_z \; ; \qquad \text{for } y = 0, \text{ and } x < 0. \tag{A-51}$$

Equation (A-51) implies that $\frac{\partial H_z^s}{\partial y} = - ik \frac{Z_s}{Z_o} H_z^s$ for $y = 0$, $x < 0$, and

$$\frac{\partial H_z}{\partial y} = 0 \qquad ; \qquad \text{for } y = 0, \text{ and } x > 0. \tag{A-52}$$

Equation (A-52) also implies that

$$\frac{\partial H_z^s}{\partial y} = - \frac{\partial H_z^i}{\partial y} \quad \text{for } y = 0, \; x > 0. \tag{A-53}$$

H_z^s satisfies the radiation condition for $e^{-i\omega t}$ time dependence.

One may next define the following Fourier transforms.

$$\hat{h}^s = \frac{1}{\sqrt{2\pi}} \int_{-\infty}^{\infty} H_z^s \, e^{isx} \, dx = \hat{h}_+^s + \hat{h}_-^s \tag{A-54a}$$

$$\hat{h}_+^s = \frac{1}{\sqrt{2\pi}} \int_0^{\infty} H_z^s \, e^{isx} \, dx \; ; \; \hat{h}_-^s = \frac{1}{\sqrt{2\pi}} \int_{-\infty}^{0} H_z^s \, e^{isx} \, dx \tag{A-54b;A-54c}$$

$$\hat{h}_+^i = \frac{1}{\sqrt{2\pi}} \int_0^{\infty} H_z^i \, e^{isx} \, dx = \frac{ie^{-\alpha y}}{\sqrt{2\pi}(s+\beta)} \; , \text{ via (A-48).} \tag{A-55}$$

H_z^s and H_z^i individually satisfy the wave equation in Equation (A-50). Fourier transforming Equation (A-50) for H_z^s instead of H_z, one obtaines

$$\left(\frac{\partial^2}{\partial y^2} + \lambda\right) \hat{h}^s = 0 \; ; \quad \lambda = \sqrt{k^2-s^2} = i\sqrt{s^2-k^2} \tag{A-56}$$

in which Im $\sqrt{\lambda>0}$. The solution to Equation (A-56) in accordance with Equation (A-53) is

$$\hat{h}^s = c(s)\, e^{i\sqrt{\lambda}\, y} \quad , \quad y \geq 0. \tag{A-57}$$

The inverse Fourier transform of $\hat{h}^s$ leads to H_z^s. Thus,

$$H_z^s = \frac{1}{\sqrt{2\pi}} \int_{-\infty}^{\infty} \hat{h}^s\, e^{-isx}\, ds \quad . \tag{A-58}$$

Incorporating Equations (A-48) and (A-58) in $H_z = H_z^i + H_z^s$ which appears in the boundary conditions (A-51) and (A-52) yields

$$\int_{-\infty}^{\infty} L^{-1}(s)\phi(s)e^{-isx}ds = 0 \quad , \quad x < 0 \quad , \tag{A-59}$$

$$\int_{-\infty}^{\infty} \phi(s)e^{-isx}ds = - i\sqrt{2\pi}\, \alpha\, e^{i\beta x} \quad , \quad x > 0 \quad , \tag{A-60}$$

where

$$\phi(s) \equiv \sqrt{\lambda}\, c(s) \tag{A-61}$$

and

$$L(s) = \frac{\sqrt{\lambda}}{\sqrt{\lambda} - i\alpha} = \frac{\sqrt{k^2-s^2}}{\sqrt{k^2-s^2} - i\alpha} \quad . \tag{A-62}$$

The above set of dual integral equations for $\phi(s)$ in Equation (A-59) and Equation (A-60) may be solved via the method of factorization [12]. Without going through the details, one obtains

$$c(s) = \frac{\alpha}{\sqrt{2\pi}} \frac{L_-(s)}{L_-(-\beta)\sqrt{k^2-s^2}(s+\beta)} \tag{A-63}$$

in which

$$L(s) = L_+(s)\, L_-(s) \tag{A-64}$$

defines the Wiener Hopf factors $L_+(s)$ and $L_-(s)$ for the $L(s)$ of Equation (A-62). $L_+(s)$ is analytic for Im $s>0$ and $L_-(s)$ is analytic for Im $s<0$. Incorporating Equation (A-63) in Equation (A-57) and employing Equation (A-58) yields

$$H_z^s = \frac{\alpha}{2\pi} \int_{-\infty}^{\infty} \frac{L_-(s)}{L_-(-\beta)} \frac{1}{(s+\beta)\sqrt{k^2-s^2}} e^{i\sqrt{k^2-s^2}\, y} e^{-isx}\, ds \quad . \tag{A-65}$$

The residue of the pole at $s=\beta$ in the integrand of Equation (A-65) furnishes the reflected surface wave for $x<0$, whereas the pole at $s=-\beta$ furnishes the negative of the incident field for $x>0$ (see Equation (A-48) where it was assumed that H_z^i exists for $|x|<\infty$), and therefore cancels the incident field for $x>0$. The reflected surface wave field is

$$H_z^{rsw} = R_H^* e^{-\alpha y - i\beta x} \quad ; \quad x < 0 \tag{A-66}$$

where

$$R_H^* = \frac{R_h}{2\beta[L_+(\beta)]^2} \quad ; \quad R_h \equiv \lim_{s\to\beta} (s-\beta)\, L(s) = \frac{\alpha^2}{\beta} \quad . \tag{A-67}$$

Clearly, R_H^* is the reflection coefficient at ($x=0$, $y=0$) associated with the reflected surface wave.

The diffracted field, H_z^d may be found from an asymptotic evaluation of the integral in Equation (A-65) via the method of steepest descent. To this end, one introduces the transformations $s=k\cos w$, $ds=-k\sin w\, dw$, $\sqrt{k^2-s^2}=k\sin w$, $x=\rho\cos\phi$ and $y=\rho\sin\phi$. Thus,

$$H_z^s = -\frac{\alpha}{2\pi} \int_{C_w} \frac{L_-(k\cos w)}{L_-(k\cos w_p)(k\cos w+\beta)} e^{-ik\rho\cos(w+\phi)}\, dw \quad . \tag{A-68}$$

The contour c_w in Equation (A-68) is indicated in Figure A-3. The contour c_w may be deformed into the steepest descent path (one notes that the pole at $s=+\beta$ which may be crossed in the path deformation yields H_z^{rsw} of Equation (A-66) and hence this pole crossing will be ignored since it's contribution has already been evaluated in Equation (A-66)). Without any details for brevity, the resulting saddle point approximation along the steepest descent path yields

$$H_z^d \sim -\frac{\alpha}{2\pi}\sqrt{\frac{2\pi}{k\rho}}\, e^{i(k\rho-\frac{\pi}{4})}\, \frac{L(-k\cos\phi)}{L_+(-k\cos\phi)L_+(k\cos w_p)(\beta-k\cos\phi)} \quad . \tag{A-69}$$

The quantity w_p in Equations (A-68) and (A-69) is related to β via

$$\beta = k\cos w_p . \tag{A-70}$$

One may rewrite Equation (A-69) as

$$H_z^d \sim D^*(\phi)\, \frac{e^{+ik\rho}}{\sqrt{\rho}} \tag{A-71}$$

where

$$D^*(\phi) = -\frac{\alpha e^{-i\frac{\pi}{4}}}{\sqrt{2\pi k}}\, \frac{L(-k\cos\phi)}{L_+(-k\cos\phi)L_+(k\cos w_p)(\beta-k\cos\phi)} \quad . \tag{A-72}$$

The explicit form of the factors $L_\pm(s)$ may be obtained conveniently from the procedures outlined in [13] or [14]. In the present instance, it has been found that the procedure given by Weinstein [14] leads to simple and useful expressions for $L_\pm(s)$. Without going through the details of obtaining $L_\pm(s)$ via the method in [14], one may directly write the expressions for R_H and $D(\phi)$ corresponding to the surface wave reflection and diffraction coefficients in the $e^{j\omega t}$ time convention in terms of the results for $L_\pm(s)$ as

$$R_H = -\frac{1-\beta/k}{\beta/k}\, e^{\frac{j}{\pi}\int_0^{2\xi} du\, \frac{u}{\sinh u}} \tag{A-73}$$

and

$$D(\phi) = \frac{e^{j\frac{\pi}{4}}}{\sqrt{2\pi k}} \frac{\sinh\xi}{\cosh\xi-\cos\phi} \sqrt{\frac{2\cosh\xi(1+\cos\phi)}{(1+\cosh\xi)(\cosh\xi+\cos\phi)}} \cdot$$

$$\cdot e^{+\frac{j}{2\pi}\int_0^{2\xi} \frac{udu}{\sinh u} + \frac{1}{2\pi}\int_{\phi+j\xi}^{\phi-j\xi} \frac{udu}{\sin u}} \qquad \text{(A-74)}$$

with

$$\xi = \sinh^{-1}\frac{\alpha}{k} \qquad \text{(A-75)}$$

It is noted that R_H and D in Equations (A-73) and (A-74) for the $e^{j\omega t}$ time dependence are the complex conjugates of R_H^* and D^* in Equation (A-67) and Equation (A-71) for the $e^{-i\omega t}$ time dependence, respectively.

TM_z case

The excitation E_z^i in this case is given by

$$E_z^i = e^{-\alpha y + i\beta x} \quad ; \quad |x| < \infty \qquad \text{(A-76)}$$

in which it is assumed that E_z^i exists even for $x > 0$.

$$\beta = k\sqrt{1 - \left(\frac{Z_o}{Z_s}\right)^2} \quad ; \quad \alpha^2 = \beta^2 - k^2 \quad (\beta > k) \,, \qquad \text{(A-77a;A-77b)}$$

as in Equations (A-40a;A-40b) for the TM_z case with $Z_s = -jX_c (X_c > 0)$ corresponding to capacitive reactance. Again an $e^{-i\omega t}$ time dependence will be employed in the analysis to follow; however, the final results will be presented for the $e^{j\omega t}$ time dependence. Let E_z and E_z^s denote the total and the scattered fields, respectively, then $E_z = E_z^i + E_z^s$. The total field E_z satisfies

$$(\nabla_t^2 + k^2) E_z = 0 \quad ; \quad \text{for } y \geq 0, \quad |x| < \infty \,, \qquad \text{(A-78)}$$

$$\frac{\partial E_z}{\partial y} = -ik\frac{Z_o}{Z_s} E_z \quad ; \quad \text{for } y = 0 \text{ and } x < 0 \,, \qquad \text{(A-79)}$$

$$E_z = 0 \quad ; \quad \text{for } y = 0 \text{ and } x > 0. \qquad \text{(A-80)}$$

E_z^s satisfies the radiation condition for $e^{-i\omega t}$ time dependence. (A-81)

One defines the Fourier transforms

$$\hat{e}^s = \frac{1}{\sqrt{2\pi}} \int_{-\infty}^{\infty} E_z^s \, e^{isx} \, dx = \hat{e}_+^s + \hat{e}_-^s \quad \text{as in (A-54a)} \tag{A-82}$$

and

$$\hat{e}_+^i = \frac{1}{\sqrt{2\pi}} \int_{0}^{\infty} E_z^i \, e^{isx} \, dx = \frac{i \, e^{-\alpha y}}{\sqrt{2\pi}(s+\beta)} \quad , \text{ via (A-76)} \quad . \tag{A-83}$$

E_z^s and E_z^i individually satisfy the wave equation in (A-78). Thus, Fourier transforming Equation (A-78) for E_z^s instead of E_z yields

$$\left(\frac{\partial^2}{\partial y^2} + \lambda \right) \hat{e}^s = 0 \quad ; \quad \lambda = \sqrt{k^2 - s^2} = i\sqrt{s^2 - k^2} \tag{A-84}$$

in which $\mathrm{Im}\sqrt{\lambda} > 0$. The solution to Equation (A-84) subject to Equation (A-81) is

$$\hat{e}^s = A(s) \, e^{i\sqrt{\lambda} y} \quad , \quad y \geq 0. \tag{A-85}$$

The inverse Fourier transform of Equation (A-85) leads to E_z^s.

$$E_z^s = \frac{1}{\sqrt{2\pi}} \int_{-\infty}^{\infty} \hat{e}^s \, e^{-isx} \, ds \quad . \tag{A-86}$$

One may incorporate Equations (A-76) and (A-86) in the boundary conditions of Equations (A-79) and (A-80) to obtain

$$\int_{-\infty}^{\infty} G^{-1}(s) A(s) \, e^{-isx} \, ds = 0, \quad x < 0 \tag{A-87}$$

$$\int_{-\infty}^{\infty} A(s) \, e^{-isx} \, ds = - \sqrt{2\pi} \, e^{i\beta x} \quad , \quad x > 0. \tag{A-88}$$

where

$$G^{-1}(s) = \sqrt{\lambda} - i\alpha = \sqrt{\lambda} \, L^{-1}(s) \quad , \quad \text{(see (A-62) for } L(s)). \tag{A-89}$$

Equations (A-87) and (A-88) are a set of dual integral equations for A(s) which may be solved via the method of factorization as in TE_z case treated earlier. Without presenting any details for the sake of brevity, the result for A(s) is given by

$$A(s) = \frac{-i}{\sqrt{2\pi}} \frac{1}{(s+\beta)} \frac{G_-(s)}{G_-(-\beta)} \quad , \tag{A-90}$$

where $G(s) = G_+(s)G_-(s)$ in which, $G_+(s)$ and $G_-(s)$ represent the Wiener-Hofp factors of G(s). The $\sqrt{\lambda}$ in Equation (A-89) may be factorized by inspection, and the factorization of L(s) is known from the TE_z case; thus the factorization of G(s) is directly obtained. One may now write Equation (A-86) as:

$$E_z^s = \frac{-i}{2\pi} \int_{-\infty}^{\infty} \frac{G_-(s)}{G_-(-\beta)} \frac{1}{(s+\beta)} e^{i\sqrt{k^2-s^2}\, y} e^{-isx}\, ds \quad . \tag{A-91}$$

As in the TE_z case, the pole of the integrand in Equation (A-91) at $s=-\beta$ yields a residue contribution only for $x>0$ which exactly cancels the incident field for $x>0$. On the other hand, the pole at $s=\beta$ yields the reflected surface wave E_z^{rsw} for $x<0$.

$$E_z^{rsw} = R_E^* e^{-\alpha y} e^{-i\beta x} \quad , \quad x < 0 \tag{A-92}$$

where

$$R_E^* = \frac{R_e}{2\beta[G_+(\beta)]^2} \quad ; \quad R_e \equiv \lim_{s\to\beta} (s-\beta)\, G(s) = -\frac{i\alpha}{\beta}. \tag{A-93}$$

R_E^* represents the reflection coefficient at (x=0, y=0) for the reflected surface wave field.

The diffracted field E_z^d may be obtained by asymptotically approximating Equation (A-91) via the method of steepest descent as done earlier for H_z^d in the TE_z problem. Thus,

$$E_z^d \sim D^*(\phi) \frac{e^{+ik\rho}}{\sqrt{\rho}} \quad , \tag{A-94}$$

where

$$D^* = \frac{ike^{-i\frac{\pi}{4}}}{\sqrt{2\pi k}} \frac{G(-k\cos\phi)\sin\phi}{G_+(-k\cos\phi)G_+(k\cos w_p)(\beta-k\cos\phi)} \quad ; \quad \beta = k\cos w_p. \tag{A-95}$$

As in the TE_z case, the surface wave reflection and diffraction coefficients R_E and D may be explicitly written down for the $e^{j\omega t}$ time convention as

$$R_E = j \frac{\sqrt{(\beta/k)^2 - 1}}{\beta/k} \; e^{\frac{j}{\pi} \int_0^{2\xi} \frac{udu}{\sinh u}} \tag{A-96}$$

and

$$D(\phi) = j \frac{e^{j\frac{\pi}{4}}}{\sqrt{2\pi k}} \left(\frac{\sin\phi}{\cosh\xi - \cos\phi} \right) \sqrt{\frac{2\cosh\xi}{\cosh\xi + \cos\phi}} \; e^{\frac{j}{2\pi} \int_0^{2\xi} \frac{udu}{\sinh u} + \frac{1}{2\pi} \int_{\phi + j\xi}^{\phi - j\xi} \frac{udu}{\sin u}} \tag{A-97}$$

where

$$\xi = \sinh^{-1} \frac{\alpha}{k} \tag{A-98}$$

and

R_E and D for the $e^{j\omega t}$ time convention are the complex conjugates of R_E^* and D* in Equations (A-93) and (A-95) for the $e^{-i\omega t}$ case, respectively.

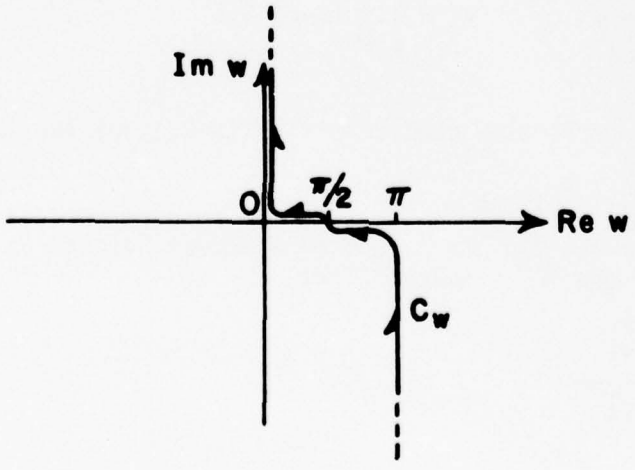

Figure A-3. Contour of integration in the complex w-plane.

APPENDIX III

SURFACE FIELDS IN THE CANONICAL PROBLEM OF A LINE SOURCE ON A CIRCULAR CYLINDER COMPLETELY COVERED WITH AN IMPEDANCE SURFACE

The geometrical configuration of the problem is illustrated in Figure 7. The line source is a magnetic current $\overline{M}$ which is either a $\hat{z}$-directed magnetic line source, or a $\hat{\phi}$-directed magnetic line dipole; as before the former represents the source for the TE_z case; whereas, the latter represents the source for the TM_z case. The TE_z case is treated first, and it is followed by the treatment of the TM_z case.

TE_z or the axial slot case

The magnetic current $\overline{M}$ at Q' in this case is

$$\overline{M} = \hat{z}\, M \frac{\delta(\rho-a)\delta(\phi)}{\rho} \quad , \tag{A-99}$$

and it generates only a $\hat{z}$-component of the magnetic field which is denoted by h_z.

$$(\nabla_t^2 + k^2)h_z = jkY_o\, M \frac{\delta(\rho-a)\delta(\phi)}{\rho} \quad ; \quad \begin{matrix} \rho \geq a \\ 0 \leq \phi \leq 2\pi \end{matrix} \quad . \tag{A-100}$$

and

$$\left[\frac{\partial h_z}{\partial \rho} - jk \frac{Z_s}{Z_o} h_z\right] = 0 \text{ at } \rho = a. \tag{A-101}$$

Also, h_z satisfies the radiation condition. Using the method of Green's functions, one may obtain the following expression for h_z:

$$h_z(\rho,\phi) = - jkY_o\, M\, G_m(\overline{\rho}|\overline{\rho}')\Big|_{\overline{\rho}'=a} \tag{A-102}$$

where $G_m(\overline{\rho}|\overline{\rho}')$ is a Green's function which satisfies the radiation condition, and

$$(\nabla_t'^2 + k^2)\, G_m(\overline{\rho}'|\overline{\rho}) = - \frac{\delta(\rho-\rho')\delta(\phi-\phi')}{\rho'}$$

in which $\overline{\rho}$ is the position vector of (ρ,ϕ); and likewise $\overline{\rho}'$ is the position vector of (ρ',ϕ'). Also,

$$\left[\frac{\partial G_m}{\partial \rho'} - j\,k\,\Delta\,G_m\right] = 0 \text{ at } \rho = a \tag{A-104}$$

with

$$\Delta = \frac{Z_s}{Z_o} \quad ; \quad Z_s = \text{value of the surface impedance which completely covers the cylinder;} \quad Z_o = \text{free space impedance.} \tag{A-105}$$

The solution to G_m may be constructed via the methods presented in [10]; thus

$$G_m(\bar{\rho}|\bar{\rho}')\Big|_{\substack{\rho'=a \\ \phi'=0}} = \frac{j}{2\pi a} \int_{-\infty-j\varepsilon}^{\infty-j\varepsilon} d\nu \, \frac{H_\nu^{(2)}(k\rho)}{\left\{\left[\frac{\partial}{\partial\rho} - jk\Delta\right] H_\nu^{(2)}(k\rho)\right\}_{\rho=a}} \, \frac{\cos\nu(\pi-|\phi|)}{\sin\nu\pi} \tag{A-106}$$

where $H_\nu^{(2)}(k\rho)$ is the cylindrical Hankel function of the second kind, and of order ν. One may write

$$\frac{\cos\nu(\pi-|\phi|)}{\sin\nu\pi} = \sum_{\ell=0}^{\infty} j\left[e^{-j\nu|\phi|} + e^{-j\nu(2\pi-|\phi|)}\right] e^{-j\nu(2\pi\ell)} \tag{A-107}$$

Physically, the above series corresponds to multiple encirclements of the field around the cylinder in the azimuthal propagation representation for Green's function G_m presented in Equation (A-106). Since one is interested in applying the results of the present analysis to perfectly conducting cylinders with a surface impedance cover of finite extent, the effects of these multiple encirclements will be neglected. Thus, for the present purposes one writes

$$G_m(\bar{\rho}|\bar{\rho}') = \tilde{G}_m(\bar{\rho}|\bar{\rho}') + \text{multiply encircling wave contributions} \tag{A-108}$$

from which it follows that

$$\tilde{G}_m(\bar{\rho}|\bar{\rho}')\Big|_{\substack{\rho'=a \\ \phi'=0}} = -\frac{1}{2\pi a} \int_{-\infty-j\varepsilon}^{\infty-j\varepsilon} d\nu \, \frac{H_\nu^{(2)}(k\rho)\left[e^{-j\nu|\phi|} + e^{-j\nu(2\pi-|\phi|)}\right]}{\left\{\left[\frac{\partial}{\partial\rho} - jk\Delta\right] H_\nu^{(2)}(k\rho)\right\}_{\rho=a}} \tag{A-109}$$

and the field h_z which corresponds to this non-encircling part is $\tilde{h}_z$. Thus,

$$\tilde{h}_z(\rho,\phi) = - jkY_o M \tilde{G}_m(\rho,\phi|a,0) \qquad \text{(A-110)}$$

represents the non-encircling part of h_z in terms of $\tilde{G}_m$, in which $\tilde{G}_m(\rho,\phi|a,0)$ is given explicitly in Equation (A-109). Let

$$\tilde{h}_z(\rho,\phi) = \tilde{h}_z^+ + \tilde{h}_z^- \qquad \text{(A-111)}$$

where the $\tilde{h}_z^+$ terms corresponds to the clockwise circumferential propagation term $e^{-j\nu|\phi|}$ in Equation (A-109), whereas $\tilde{h}_z^-$ corresponds to the counter-clockwise circumferentially propagating term $e^{-j\nu(2\pi-|\phi|)}$ in Equation (A-109). Defining

$$\psi^{\pm} = \left\{ \begin{matrix} |\phi| \\ 2\pi-|\phi| \end{matrix} \right\}; \quad \xi^{\pm} = m\psi^{\pm} \quad ; \; m = \left(\frac{ka}{2}\right)^{1/3} \qquad \text{(A-112;A-113;A-114)}$$

and assuming that ka is sufficiently large, one may approximate G_m and hence $\tilde{h}_z^{\pm}$ on the surface $\rho=a$, within the shadow region of the source at Q' ($\rho=a$, $\phi=0$) as

$$\tilde{h}_z^{\pm}\Big|_{\rho=a} \approx c_o M \left[e^{-jka\psi^{\pm}} \sqrt{\frac{jk}{2\pi}} \cdot \frac{1}{m} \int_{-\infty}^{\infty} d\tau \, \frac{w_2(\tau) e^{-j\xi^{\pm}\tau}}{w_2'(\tau)+jm\frac{Z_s}{Z_o} w_2(\tau)} \right] \qquad \text{(A-115)}$$

in which

$$c_o \equiv - \sqrt{\frac{jk}{8\pi}} \, Y_o \qquad \text{(A-116)}$$

and

$$H_\nu^{(2)}(ka) \sim \frac{j}{m\sqrt{\pi}} w_2(\tau); \quad \frac{\partial}{\partial\rho} H_\nu^{(2)}(k\rho) \sim - \frac{jk}{m\sqrt{\pi}} w_2'(\tau). \qquad \text{(A-117a;A-117b)}$$

The variables ν and τ are related through the transformation:

$$\tau = \frac{\nu - ka}{m} . \qquad \text{(A-117c)}$$

$w_2(\tau)$, and $w_2'(\tau)$ are the Fock type Airy functions defined in [5] (also see [6]). If the surface impedance Z_s is inductively reactive, then the large curved impedance surface will support an Elliot type mode mentioned in Sections I and II. The field of this Elliot mode is obtained by evaluating the residue of the integrand in Equation (A-115) at $\tau=\tau_o$ which locates the Elliot mode pole of

$$\frac{1}{w_2'(\tau)+jm\frac{Z_s}{Z_o}w_2(\tau)} \quad .$$

Thus,

$$w_2'(\tau_o) + j\, m \frac{Z_s}{Z_o} w_2(\tau_o) = 0, \quad \text{at } \tau=\tau_o \quad . \tag{A-118}$$

While several papers have been written on the solution for τ_o in Equation (A-118), the one which appears to have dealt with this problem in great detail is due to Logan [5]; and, Logan's results are used in the present work. The value of τ_o is approximately given by [5]

$$\tau_o \approx (q^2 + \frac{1}{2q} + \frac{1}{8q^4} + \frac{5}{32q^7} + \frac{11}{32q^{10}}) + j\, 2q^2\, e^{-(4/3)q^3}; \quad q>>2, \tag{A-119}$$

where

$$q = - jm \frac{Z_s}{Z_o} \quad . \tag{A-120}$$

In addition to the root $\tau=\tau_o$ corresponding to the Elliot mode, there are other roots of the equation in (A-118) which correspond to the set of Watson modes which are characterized by a significant exponential decay along their propagation paths. One is primarily interested in the Elliot mode field in this study as mentioned in Section II-B, hence the Watson type modes will not be discussed. Evaluating the residue at $\tau=\tau_o$ yields the Elliot mode field corresponding to $\tilde{h}_z^{\pm}$ as:

$$\tilde{h}_z^{\pm}(a,\phi) = - \frac{kY_oM}{2m} \frac{e^{-j(k + \frac{m}{a}\tau_o)a\psi^{\pm}}}{\left(\tau_o + \left[m \frac{Z_s}{Z_o}\right]^2\right)} \tag{A-121}$$

which may be rewritten as

$$\tilde{h}_z^{\pm} = c_o\, M\, L^{ew}\, e^{-j\gamma t_1^2} \quad ; \quad t_1 \equiv a\psi^{\pm} \quad . \tag{A-122}$$

The quantities L^{ew} and γ are given by:

$$L^{ew} = 8\pi jk \cdot \frac{-j}{2m} \cdot \left[\frac{1}{\tau_o + \left[m \frac{Z_s}{Z_o} \right]^2} \right], \qquad \text{(A-123)}$$

and

$$\gamma = k + \frac{m}{a} \tau_o \quad , \qquad \text{(A-124)}$$

in which m and τ_o were previously defined in Equation (A-114) and Equation (A-119), respectively. c_o is defined in Equation (A-116).

The space wave, or the field directly radiated by the source may be found by a stationary phase evaluation of the integral in Equation (A-106) for the lit region after replacing $\cos\nu[\pi-|\phi|]$ in Equation (A-106) by $e^{-j\nu\pi}\cos\nu\phi + je^{j\nu|\phi|}\sin\nu\pi$, and by including only the term $e^{j\nu|\phi|}\sin\nu\pi$ in this asymptotic, stationary phase evaluation. The other term $e^{-j\nu\pi}\cos\nu\phi$ gives rise to diffraction contributions arising from the multiply encircling circumferentially propagating modes which are not of interest in this analysis as discussed earlier in the evaluation of $\tilde{G}_m$ or $\tilde{h}_z^{\pm}$ in Equation (A-109) and Equation (A-110). This stationary phase evaluation leads to the geometrical optics approximation for the field directly radiated by the slot as

$$\tilde{h}_z\Big|_{\text{lit region}} \sim c_o M R(\phi) \frac{e^{-jks'}}{\sqrt{s'}} \quad ; \quad \begin{array}{l} s'=Q'P \\ Q' \text{ is at } (a,0) \\ P \text{ is at } (\rho,\phi). \end{array} \qquad \text{(A-125)}$$

where c_o is as in Equation (A-116), and $R(\phi)$ is the same as in Equation (A-26) for the planar case with the exception that ϕ in Equation (A-125) above is the complement of the angle ϕ in Equation (A-26) due to a rotation of the coordinate systems in Figures 4 and 6 (or 7).

TM_z or the circumferential slot case

The magnetic current $\overline{M}$ at Q' in this case is

$$\overline{M} = \hat{\phi} M \frac{\delta(\rho-a)\delta(\phi)}{\rho} \quad ,$$

which is a magnetic line dipole at Q', and it generates only a $\hat{z}$-component of the electric field which is denoted by e_z. The field e_z may be expressed in terms of a Green's function $G_e(\overline{\rho'}|\overline{\rho})$ which satisfies the radiation condition, the partial differential equation in (A-103), and the boundary condition in Equation (A-106) with

$$\Delta \equiv \frac{Y_s}{Y_o} = \frac{Z_o}{Z_s} \quad . \tag{A-126}$$

The Δ in Equation (A-126) is now the reciprocal of that in Equation (A-105). The field $e_z(a,\phi)$ on the surface of the impedance covered cylinder may be shown to be related to $G_e(\bar{\rho}|\bar{\rho}')$ by

$$e_z(a,\phi) = -\hat{\phi}\, M\nabla x\, \hat{z} G_e(\bar{\rho}|\bar{\rho}') \Big|_{\substack{\bar{\rho}' \to (a,0) \text{ at } Q' \text{ on surface} \\ \bar{\rho} \to (a,\phi) \text{ at } P \text{ on surface.}}} \tag{A-127}$$

or

$$e_z(a,\phi) = j\frac{kM}{2\pi a} \int_{-\infty-j\varepsilon}^{\infty-j\varepsilon} d\nu \frac{H_\nu^{(2)'}(ka)}{\left\{\left[\frac{\partial}{\partial\rho} - jk\Delta\right] H_\nu^{(2)}(k\rho)\right\}_{\rho=a}} \frac{\cos\nu(\pi-|\phi)}{\sin\nu\pi} \tag{A-128}$$

As before, employing Equation (A-107) and neglecting the multiply encircling terms in e_z, one obtains $\tilde{e}_z$ which excludes the effects of the multiple encirclements as

$$e_z = \tilde{e}_z + \text{multiply encircling terms} \tag{A-129}$$

where

$$\tilde{e}_z(a,\phi) = -\frac{kM}{2\pi a} \int_{-\infty-j\varepsilon}^{\infty-j\varepsilon} d\nu \frac{H_\nu^{(2)'}(ka)}{\left\{\left[\frac{\partial}{\partial\rho} - jk\Delta\right] H_\nu^{(2)}(k\rho)\right\}_{\rho=a}} \left[e^{-j\nu|\phi|} + e^{-j\nu(2\pi-|\phi|)}\right]. \tag{A-130}$$

One may further express $\tilde{e}_z$ as

$$\tilde{e}_z(a,\phi) = \tilde{e}_z^{+} + \tilde{e}_z^{-} \tag{A-131}$$

in which $\tilde{e}_z^{+}$ corresponds to the $e^{-j\nu|\phi|}$ term and $\tilde{e}_z^{-}$ corresponds to the $e^{-j\nu(2\pi-|\phi|)}$ term in Equation (A-130). Then introducing the quantities, $\psi^{\pm}$, $\xi^{\pm}$ and m as in Equations (A-112;A-113;A-114), and the Fock approximations for $H_\nu^{(2)}(ka)$ in Equations (A-117a;A-117b), respectively, one obtains:

$$\tilde{e}_z^{\pm} \approx c_o \frac{Z_s}{Z_o} M \left[- e^{-jka\psi^{\pm}} \sqrt{\frac{jk}{2\pi}} \frac{1}{m^3} \int_{-\infty}^{\infty} d\tau \frac{w_2'(\tau) e^{-j\xi^{\pm}\tau}}{w_2(\tau) - j\left(m \frac{Z_o}{Z_s}\right)^{-1} w_2'(\tau)} \right] \quad \text{(A-132)}$$

in which

$$c_o = -\sqrt{\frac{jk}{8\pi}} \quad . \quad \text{(A-133)}$$

If the surface impedance Z_s is purely capacitive, then the large curved impedance surface will support an Elliot type mode mentioned in Sections I and II. The Elliot mode corresponds to the value of $\tau=\tau_o$ for which

$$w_2'(\tau_o) + j\, m \frac{Z_o}{Z_s} w_2(\tau_o) = 0. \quad \text{(A-134)}$$

This value, $\tau=\tau_o$ corresponds to the location of the pole of the Elliot mode in the integrand of Equation (A-132). The root $\tau=\tau_o$ is obtained via Equation (A-119) given by Logan [5] with

$$q = - j\, m \frac{Z_o}{Z_s} \quad . \quad \text{(A-135)}$$

Other roots of Equation (A-134) corresponding to a set of Watson modes will not be discussed due to reasons mentioned in Section II. Evaluating the residue at $\tau=\tau_o$ in Equation (A-132) leads to the following result for the Elliot mode field.

$$\tilde{e}_z^{\pm}(a,\phi) = \frac{kM}{2m} \frac{Z_o}{Z_s} \frac{e^{-j(k + \frac{m}{a}\tau_o)a\psi^{\pm}}}{\left(\tau_o + \left[m \frac{Z_o}{Z_s}\right]^2\right)} \quad , \quad \text{(A-136)}$$

which may be rewritten as

$$\tilde{e}_z^{\pm}(a,\phi) = c_o M L^{ew} e^{-j\gamma t_1^2} \quad ; \quad t_1 = a\psi^{\pm} \quad . \quad \text{(A-137)}$$

The quantities L^{ew} and γ are given by

$$L^{ew} = \sqrt{8\pi jk} \cdot j \frac{Z_o}{Z_s} \cdot \frac{1}{2m} \cdot \left[\frac{1}{\tau_o + \left[m \frac{Z_o}{Z_s} \right]^2} \right] \qquad \text{(A-138)}$$

and

$$\gamma = k + \frac{m}{a} \tau_o \quad . \qquad \text{(A-139)}$$

The c_o in Equation (A-137) is defined previously in Equation (A-133), and τ_o is as in Equation (A-119) with q as in Equation (A-135).

The evaluation of the field directly radiated by the source in the lit region is not described since it reduces to the geometrical optics approximation as in the TE_z case. Denoting this result for $e_z(\rho,\phi)$ by $\tilde{e}_z(\rho,\phi)\Big|_{\text{lit region}}$, one may write

$$\tilde{e}_z(\rho,\phi)\Big|_{\text{lit region}} \sim c_o M R(\phi) \frac{e^{-jks'}}{\sqrt{s'}} ; \qquad \begin{array}{l} Q'P = s' \\ Q' \text{ is at } (a,0) \\ P \text{ is at } (\rho,\phi). \end{array} \qquad \text{(A-140)}$$

in which c_o is as in Equation (A-137), and $R(\phi)$ is the same as in Equation (A-45) for the planar TM_z case except that the ϕ in Equation (A-140) is the complement of the angle ϕ in Equation (A-45) due to a rotation of the coordinate systems in Figures 4 and 6 (or 7).

APPENDIX IV

THE RADIATION BY AN EQUIVALENT LINE SOURCE AT A DISCONTINUITY IN SURFACE IMPEDANCE ON A PERFECTLY CONDUCTING CIRCULAR CYLINDER COVERED WITH A SURFACE IMPEDANCE PATCH

The geometry of this problem is illustrated in Figure 8. Specifically, the problem is to obtain an approximate but accurate expression for the fields $\tilde{u}_1^{sd}$ and $\tilde{u}_1^{d}$ which are produced via diffraction of the incident field u^i from Q_1. A similar set of diffracted fields $\tilde{u}_2^{sd}$ and $\tilde{u}_2^{d}$ are also produced via diffraction of $\tilde{u}^i$ from Q_2, but for the sake of definiteness, one may analyze only the diffraction from Q_1 in this appendix; the results for the diffraction from Q_2 would be similar to those for the diffraction from Q_1. For an electrically large cylinder, the diffracted field $\tilde{u}_1^{d}$ on the lit side of SBQ_1 in the deep lit region is taken to be characterized by the same diffraction coefficient as in the field $\tilde{u}^d$ which occurs in the problem of surface wave diffraction by a two part impedance surface of Figure 5. The diffraction coefficient D is defined in Equation (A-74) for the TE_z case, and in Equation (A-97) for the TM_z case, in Appendix II. Thus, $\tilde{u}_1^{d}$ may be written as in Equation (20).

$$\tilde{u}_1^{d}(P) \sim \tilde{u}^{i}(Q_1)\, D(\delta_1)\, \frac{e^{-jks_1}}{\sqrt{s_1}} \quad ; \quad s_1 = Q_1P \text{ and P is on the lit side of } SBQ_1 \text{ in the deep lit region.} \tag{A-141}$$

The field $\tilde{u}_1^{d}(P)$ may be assumed to be produced by an equivalent magnetic line current $\overline{M}^{eq}$ at Q_1 on a perfectly conducting or "unperturbed" cylinder; i.e., on the same cylinder as in Figure 8, but without the surface impedance patch. Once $\overline{M}^{eq}$ is found, it may be systematically employed to obtain the field $\tilde{u}_1^{sd}$ on the shadow side of SBQ_1. The TE_z or the axial slot case will be analyzed first; the TM_z or the circumferential slot case will be analyzed subsequently.

TE_z case

The magnetic field is entirely $\hat{z}$-directed in this case, thus the field $\tilde{u}_1^{d}(P)$ in Equation (A-141) may be considered to be produced by a z-directed magnetic line source $\overline{M}^{eq}$ at Q' on the "unperturbed" cylinder as mentioned above. In this case, $\overline{M}^{eq}$ is given by

$$\overline{M}^{eq} = \hat{z}\, M_1^{eq}\, \frac{\delta(\rho-a)\delta(\phi-\phi_0)}{\rho} \quad , \quad \text{at } Q_1 \ . \tag{A-142}$$

The $\hat{z}$-directed magnetic field produced by $\overline{M}^{eq}$ of Equation (A-142) at Q' on the unperturbed cylinder may be easily found to be given by [6]

$$2\, c_o\, M_1^{eq}\, R^{eq}(\delta_1)\, \frac{e^{-jks_1}}{\sqrt{s_1}} \quad ; \quad s_1 = Q_1P, \text{ and P is on the lit side of } SBQ_1 \text{ in the deep lit region} \qquad \text{(A-143)}$$

where

$$c_o \equiv -\sqrt{\frac{jk}{8\pi}}\; Y_o \quad ; \quad \text{and } R^{eq}(\delta_1) = 1 \qquad \text{(A-144a;A-144b)}$$

Comparing the RHS of Equation (A-141) with Equation (A-143), one obtains

$$M_1^{eq} = \frac{\tilde{u}^i(Q_1)}{2\, c_o}\, D(\delta_1) \equiv M_1^{eq}(\delta_1) \quad . \qquad \text{(A-145)}$$

in which $\tilde{u}^i(Q_1)$ and $D(\delta_1)$ are given in Equation (15) (also see Equations (A-123) and (A-124)) and (A-74), respectively. Consequently, M_1^{eq} depends on the aspect angle δ_1, however this is acceptable since $\overline{M}^{eq}$ is only an equivalent line source. The value of $M_1^{eq}(\delta_1)$ at $\delta_1=0$ would provide the strength of the equivalent source which launches the surface ray modes corresponding to $\tilde{u}_1^{cw}$ shown in Figure 8. The diffraction from the surface ray modes in turn produces the field $\tilde{u}_1^{sd}$ as in Figure 8. Thus, $\tilde{u}_1^{sd}$ may be directly obtained via the results in [6] as indicated in Equation (22).

$$\tilde{u}_1^{sd} \sim c_o\, M_1^{eq}(o) \sum_{p=1}^{N} L_p(Q_1)\, e^{-[\alpha_p + jk]\ell_1}\, D_p(T_1)\, \frac{e^{-jks_1}}{\sqrt{s_1}} \quad ;$$

P in the deep shadow region on the shadow side of SBQ_1; $\ell_1=Q_1T_1$; see Figure 8, (A-146)

where

$$L_p(Q_1) = -\, j\left(jk\,\frac{\pi}{2}\right)^{1/2} H^{(2)}_{\nu_p}(ka)\, D_p, \qquad \text{(A-147)}$$

and L_p, D_p, and α_p respectively correspond to L_p^h, D_p^h, and α_p^h in [6]. In the transition region adjacent to the shadow boundary SBQ_1, one must employ the Fock approximation in terms of $g(\cdot)$ as indicated in Equations (24) and (25).

TM_z case

The electric field is entirely $\hat{z}$-directed in this case, thus the field $\tilde{u}_1^{sd}(P)$ in Equation (A-141) may be considered to be produced by a $\hat{\phi}_o$ directed magnetic line dipole $\overline{M}^{eq}$ at Q' on the "unperturbed" cylinder as mentioned above. Thus, in this case, $\overline{M}^{eq}$ is given by:

$$\overline{M}^{eq} = \hat{\phi}_o \, M_1^{eq} \, \frac{\delta(\rho-a)\delta(\phi-\phi_o)}{\rho} \quad , \quad \text{at } Q_1. \tag{A-148}$$

The $\hat{z}$-directed electric field produced by $\overline{M}^{eq}$ in Equation (A-148) at Q' on the unperturbed cylinder is known to be [6]

$$2 \, c_o \, M_1^{eq} \, R^{eq}(\delta_1) \, \frac{e^{-jks_1}}{\sqrt{s_1}} \quad ; \quad s_1 = Q_1P \text{ and P is on the lit side of } SBQ_1 \text{ in the deep lit region,} \tag{A-149}$$

where

$$c_o \equiv -\sqrt{\frac{jk}{8\pi}} \quad ; \quad \text{and } R^{eq}(\delta_1) = \sin\delta_1 \quad . \tag{A-150);(A-151}$$

One may now find M_1^{eq} by comparing Equation (A-149) with the RHS of Equation (A-141). Thus,

$$M_1^{eq} = \frac{\tilde{u}^i(Q_1)}{2 \, c_o} \, \frac{D(\delta_1)}{\sin\delta_1} \quad , \tag{A-152}$$

in which $\tilde{u}^i(Q_1)$ and $D(\delta_1)$ are given in Equation (15) (also see Equations (A-138) and (A-139)) and (A-97), respectively. Thus, M_1^{eq} in Equation (A-152) is also dependent on δ_1 just as for the TE_z case discussed earlier. Following a similar line of reasoning as indicated for the TE_z case, the value of M_1^{eq} at $\delta_1=0$ provides the strength of the equivalent source which produces the field $\tilde{u}_1^{sd}$ in the deep shadow region on the shadow side of SBQ_1 as shown in Figure 8. One notes from Equation (A-152) that

$$M_1^{eq}\Big|_{\delta_1=0} = \lim_{\delta_1 \to 0} \frac{\tilde{u}^i(Q_1)}{2 \, c_o} \, \frac{D(\delta_1)}{\sin\delta_1} = \frac{\tilde{u}^i(Q_1)}{2 \, c_o} \cdot \left[\frac{\partial D(\delta_1)}{\partial \delta_1}\right]_{\delta_1=0} \quad . \tag{A-153}$$

It is noted from Equation (A-97) however that $D(\delta_1)$ is explicitly proportional to $\sin\delta_1$ and hence the value of $M_1^{eq}(\delta_1=0)$ is trivially calculated. Finally, from [6],

$$\tilde{u}_1^{sd}(P) \sim c_o M_1^{eq}(o) \sum_{P=1}^{N} L_p(Q_1) e^{-[\alpha_p + jk]\ell_1} D_p(T_1) \frac{e^{-jks_1}}{\sqrt{s_1}} \quad ;$$

P in the deep shadow region on the shadow side of SBQ_1; $\ell_1 = Q_1T_1$; see Figure 8, (A-154)

where

$$L_p(Q_1) = - (jk \frac{\pi}{2})^{1/2} H_{\nu_p}^{(2)'}(ka) D_p, \qquad (A\text{-}155)$$

and L_p, D_p, and α_p respectively correspond to L_p^s, D_p^s and α_p^s in [6]. In the transition region adjacent to SBQ_1 one must employ the Fock approximation in terms of $\tilde{g}(\cdot)$ as indicated in Equations (24) and (25).

METRIC SYSTEM

BASE UNITS:

Quantity	Unit	SI Symbol	Formula
length	metre	m	...
mass	kilogram	kg	...
time	second	s	...
electric current	ampere	A	...
thermodynamic temperature	kelvin	K	...
amount of substance	mole	mol	...
luminous intensity	candela	cd	...

SUPPLEMENTARY UNITS:

plane angle	radian	rad	...
solid angle	steradian	sr	...

DERIVED UNITS:

Acceleration	metre per second squared	...	m/s
activity (of a radioactive source)	disintegration per second	...	(disintegration)/s
angular acceleration	radian per second squared	...	rad/s
angular velocity	radian per second	...	rad/s
area	square metre	...	m
density	kilogram per cubic metre	...	kg/m
electric capacitance	farad	F	A·s/V
electrical conductance	siemens	S	A/V
electric field strength	volt per metre	...	V/m
electric inductance	henry	H	V·s/A
electric potential difference	volt	V	W/A
electric resistance	ohm		V/A
electromotive force	volt	V	W/A
energy	joule	J	N·m
entropy	joule per kelvin	...	J/K
force	newton	N	kg·m/s
frequency	hertz	Hz	(cycle)/s
illuminance	lux	lx	lm/m
luminance	candela per square metre	...	cd/m
luminous flux	lumen	lm	cd·sr
magnetic field strength	ampere per metre	...	A/m
magnetic flux	weber	Wb	V·s
magnetic flux density	tesla	T	Wb/m
magnetomotive force	ampere	A	...
power	watt	W	J/s
pressure	pascal	Pa	N/m
quantity of electricity	coulomb	C	A·s
quantity of heat	joule	J	N·m
radiant intensity	watt per steradian	...	W/sr
specific heat	joule per kilogram-kelvin	...	J/kg·K
stress	pascal	Pa	N/m
thermal conductivity	watt per metre-kelvin	...	W/m·K
velocity	metre per second	...	m/s
viscosity, dynamic	pascal-second	...	Pa·s
viscosity, kinematic	square metre per second	...	m/s
voltage	volt	V	W/A
volume	cubic metre	...	m
wavenumber	reciprocal metre	...	(wave)/m
work	joule	J	N·m

SI PREFIXES:

Multiplication Factors	Prefix	SI Symbol
1 000 000 000 000 = 10^{12}	tera	T
1 000 000 000 = 10^{9}	giga	G
1 000 000 = 10^{6}	mega	M
1 000 = 10^{3}	kilo	k
100 = 10^{2}	hecto*	h
10 = 10^{1}	deka*	da
0.1 = 10^{-1}	deci*	d
0.01 = 10^{-2}	centi*	c
0.001 = 10^{-3}	milli	m
0.000 001 = 10^{-6}	micro	μ
0.000 000 001 = 10^{-9}	nano	n
0.000 000 000 001 = 10^{-12}	pico	p
0.000 000 000 000 001 = 10^{-15}	femto	f
0.000 000 000 000 000 001 = 10^{-18}	atto	a

* To be avoided where possible

MISSION
of
Rome Air Development Center

RADC plans and conducts research, exploratory and advanced development programs in command, control, and communications (C^3) activities, and in the C^3 areas of information sciences and intelligence. The principal technical mission areas are communications, electromagnetic guidance and control, surveillance of ground and aerospace objects, intelligence data collection and handling, information system technology, ionospheric propagation, solid state sciences, microwave physics and electronic reliability, maintainability and compatibility.

Printed by
United States Air Force
Hanscom AFB, Mass. 01731